APPLIED SCIENCES AND ENGINEERING

Nanowired human cardiac organoid transplantation enables highly efficient and effective recovery of infarcted hearts

Yu Tan[1]†, Robert C. Coyle[1]†, Ryan W. Barrs[1]†, Sophia E. Silver[1], Mei Li[1], Dylan J. Richards[1]‡, Yiliang Lin[2], Yuanwen Jiang[2], Hongjun Wang[3], Donald R. Menick[4], Kristine Deleon-Pennell[4], Bozhi Tian[2], Ying Mei[1,5]*

Human cardiac organoids hold remarkable potential for cardiovascular disease modeling and human pluripotent stem cell–derived cardiomyocyte (hPSC-CM) transplantation. Here, we show cardiac organoids engineered with electrically conductive silicon nanowires (e-SiNWs) significantly enhance the therapeutic efficacy of hPSC-CMs to treat infarcted hearts. We first demonstrated the biocompatibility of e-SiNWs and their capacity to improve cardiac microtissue engraftment in healthy rat myocardium. Nanowired human cardiac organoids were then engineered with hPSC-CMs, nonmyocyte supporting cells, and e-SiNWs. Nonmyocyte supporting cells promoted greater ischemia tolerance of cardiac organoids, and e-SiNWs significantly improved electrical pacing capacity. After transplantation into ischemia/reperfusion–injured rat hearts, nanowired cardiac organoids significantly improved contractile development of engrafted hPSC-CMs, induced potent cardiac functional recovery, and reduced maladaptive left ventricular remodeling. Compared to contemporary studies with an identical injury model, greater functional recovery was achieved with a 20-fold lower dose of hPSC-CMs, revealing therapeutic synergy between conductive nanomaterials and human cardiac organoids for efficient heart repair.

INTRODUCTION

Heart disease is the leading cause of mortality worldwide (*1*). Because of the negligible regenerative capacity of adult human hearts (*2*), cell-based therapies have been extensively explored to promote cardiac repair (*3*–*5*). From these efforts, human pluripotent stem cell–derived cardiomyocytes (hPSC-CMs) have emerged as an attractive cell source (*6*–*8*), as they can remuscularize infarcted hearts and restore contractile functions in mice (*9*), rats (*10*), guinea pigs (*11*, *12*), pigs (*13*, *14*), and nonhuman primates (*15*–*17*). However, transplantation of hPSC-CMs is conventionally performed with intramyocardial injections of dissociated cells, which results in low cell survival, moderate functional recovery, arrhythmogenic risk, and poor scalability (*18*, *19*). These fundamental obstacles limit the therapeutic potential of hPSC-CMs for cardiac repair.

The restorative capacity of hPSC-based organoid transplantation has been demonstrated in the intestine (*20*–*22*), pancreas (*23*, *24*), liver (*24*), retina (*25*), brain (*26*, *27*), and lung (*28*). Human cardiac organoids have proven to be an excellent platform for modeling human cardiac disease and drug cardiotoxicity (*29*); however, their therapeutic potential to treat infarcted hearts requires further investigation. Cardiac patches have been developed with success by several groups to treat myocardial infarction in rats (*30*–*32*) and pigs (*13*, *33*), but these often require complex fabrication methods and invasive surgical procedures. Alternatively, three-dimensional (3D) aggregates of cardiac cells, or cardiac microtissues, are known to improve cell retention after transplantation compared to dissociated cells (*34*), are less susceptible to ischemic strain than cardiac patches (*11*, *35*), and can be delivered through less invasive syringe- or catheter-based methods due to their injectable size (*36*, *37*). Our group has developed scaffold-free cardiac organoids composed of a defined ratio of hPSC-CMs, human cardiac fibroblasts (hcFBs), endothelial cells, and stromal cells. These cells self-assemble to form organoids that recapitulate fundamental cardiac tissue–level functions and contain lumenized vascular networks that reduce apoptosis during oxygen deprivation (*38*). Thus, human cardiac organoids may serve as a more robust platform for hPSC-CM transplantation in ischemic myocardium than conventional approaches.

Electrically conductive nanomaterials have been used in cardiac tissue engineering to enhance scaffold conductivity and improve the contractile properties of engineered cardiac tissues (*30*, *39*, *40*). Compared to other electrically conductive nanomaterials (e.g., gold nanowires and carbon nanotubes), electrically conductive silicon nanowires (e-SiNWs) have distinct advantages, including their biocompatibility and biodegradability (*41*, *42*), controllable electrical conductivity, tunable dimensions, and convenient surface tailorability (*43*). Our laboratory has pioneered the use of e-SiNWs to facilitate the self-assembly of hPSC-CMs into nanowired hPSC-CM spheroids (100% hPSC-CMs) with enhanced contractile function over unwired spheroids (*44*, *45*). Thus, e-SiNWs

[1]Bioengineering Department, Clemson University, Clemson, SC 29634, USA. [2]Department of Chemistry, The James Franck Institute and the Institute for Biophysical Dynamics, The University of Chicago, Chicago, IL 60637, USA. [3]Department of Surgery, Medical University of South Carolina, Charleston, SC 29425, USA. [4]Division of Cardiology, Department of Medicine, Gazes Cardiac Research Institute, Ralph H. Johnson Veterans Affairs Medical Center, Medical University of South Carolina, Charleston, SC 29425, USA. [5]Department of Regenerative Medicine and Cell Biology, Medical University of South Carolina, Charleston, SC 29425, USA.
*Corresponding author. Email: mei@clemson.edu
†These authors contributed equally to this work.
‡Present address: Immunology Translational Sciences, Janssen Research and Development LLC, 1400 McKean Rd., Spring House, PA 19477, USA.

have excellent potential as conductive nanoscaffold materials to augment human cardiac organoid transplantation.

Here, we show that nanowired hPSC-CM spheroids significantly improve hPSC-CM retention and engraftment after intramyocardial injection to healthy myocardium when compared to dissociated hPSC-CMs. We developed nanowired human cardiac organoids composed of hPSC-CMs, hcFBs, endothelial cells, stromal cells, and e-SiNWs to enhance the engraftment of nanowired human cardiac microtissues in ischemic myocardium. Multicellular nanowired organoids exhibited greater ischemia tolerance than monocellular hPSC-CM spheroids and e-SiNWs improved electrical pacing compared to unwired organoids in vitro. After injection into infarcted rat hearts, nanowired organoids accelerated the contractile development of engrafted hPSC-CMs, promoted graft vascularization, and elicited quicker and more significant recovery of cardiac function compared to unwired organoids, which correlated with enhanced mitigation of maladaptive left ventricular (LV) remodeling. These findings demonstrate synergy between human cardiac organoids and electrically conductive nanomaterials to advance the efficiency and therapeutic efficacy of hPSC-CM transplantation, a leading candidate cell therapy to treat human heart disease.

RESULTS

e-SiNWs are biocompatible with rat myocardium

We previously demonstrated that n-type doped e-SiNWs (n-type SiNWs: diameter ≈ 100 nm, length ≈ 10 μm, and silane/phosphine = 500; Fig. 1A) exhibit minimal toxicity to hPSC-CMs in vitro (*44*, *46*). In this study, in vivo cardiac biocompatibility of e-SiNWs was established by performing intramyocardial injection of 5 million e-SiNWs in healthy adult rats (Fig. 1B). Histological analysis revealed a decline in e-SiNW retention in the heart between 1 day and 7 days after injection, and after 28 days, few e-SiNWs were found (Fig. 1, C, D, and H). This could be attributed to clearance from the heart by macrophages, as evidenced by e-SiNW uptake by CD68-positive macrophages in the heart at day 7 (fig. S1). Neutrophil and macrophage infiltration decreased between days 1 and 7 after injection and was absent from the heart by day 28 (Fig. 1, E, F, I, and J). Fibroblast infiltration at the injection site also dissipated from days 1, 7, and 28 (Fig. 1, G and K). These results demonstrate that intramyocardial injection of e-SiNWs induces minimal toxicity to adult myocardium and does not elicit a chronic foreign body response in the heart.

The function of healthy adult rat hearts injected with 5 million e-SiNWs or phosphate-buffered saline (PBS) (control) was examined using electrocardiogram (ECG) and echocardiography on days −1, 1, 7, and 28 after injection (fig. S2). ECG results revealed no detectable cardiac arrhythmias after e-SiNW injection (fig. S2A), indicating that the injected e-SiNWs did not significantly affect the electrical conduction system of adult rat myocardium. In addition, left ventricle ejection fraction and fractional shortening (FS) were not significantly affected by e-SiNW injection and were found to be similar to that of the PBS-injected control rats (fig. S2, B to D). Therefore, e-SiNWs did not alter normal cardiac function after a high-dose injection into adult rat myocardium. Furthermore, total white blood cell counts were in a normal physiological range in rats injected with e-SiNWs or PBS (fig. S3 and table S1), and rats followed a normal growth curve, heart rate, and body temperature (fig. S4). Together, these results indicate that e-SiNWs are biocompatible and may be safely used in cardiac cell therapy.

Nanowired human cardiac spheroids augment engraftment of hPSC-CMs in adult rat myocardium

In our previous work, we demonstrated that e-SiNW incorporation improves human cardiac spheroid function in vitro (*46*). Here, we developed injectable nanowired hPSC-CM spheroids to investigate the effects of e-SiNW incorporation and 3D microtissue configuration on hPSC-CM transplantation (Fig. 2A). We fabricated nanowired hPSC-CM spheroids (100% hPSC-CMs) containing ~1000 hPSC-CMs and ~1000 e-SiNWs per spheroid using our previously established method (*44*) (Fig. 2, B and C). Consistent with our previous work (*46*), nanowired hPSC-CM spheroids exhibited contractile development after 7-day culture over the day 0 spheroids, as evidenced by expression of the contractile proteins sarcomeric α-actinin (αSA) (Fig. 2D) and troponin I (TnI) (Fig. 2E).

For nanowired hPSC-CM spheroid transplantation, healthy adult athymic rats were selected to study hPSC-CM engraftment and integration without confounding factors presented in cardiac injury models (*47*). Intramyocardial injection of nanowired hPSC-CM spheroids (~30×10^3 hPSC-CMs per rat) was performed to examine the engraftment of individual hPSC-CM spheroids with the host myocardium. Intramyocardial injection of dissociated hPSC-CMs was used as a control. Injecting nanowired hPSC-CM spheroids did not interfere with the electrical conduction system or normal function of the rat hearts (fig. S5). Nanowired hPSC-CM spheroids, identified by human nuclear antigen (HNA), remained aggregated 1 day after injection, resulting in enhanced cell retention compared to dissociated hPSC-CMs. This correlated with a significantly greater number of apoptotic [i.e., terminal deoxynucleotidyl transferase–mediated deoxyuridine triphosphate nick end labeling (TUNEL)–positive] cells in the dissociated hPSC-CM injection as opposed to nanowired hPSC-CM spheroids (Fig. 2, H and I). Lack of viable dissociated hPSC-CMs after injection is consistent with the literature and was attributed to injection-induced and/or anoikis-mediated cell death (*48*). At 7 days after transplantation, grafted spheroids began to lose their spherical shape and show evidence of alignment with the host myocardium (Fig. 2, J and K). Spheroids with or without nanowires exhibited contractile development at day 7 as evidenced by TnI staining (fig. S6, A and C). However, nanowired spheroids had more distinct sarcomeric banding compared to unwired spheroids (fig. S6, B and D), and a significantly greater number of nanowired spheroid grafts (fig. S6E) with greater average graft size (fig. S6F) were found at day 7 after transplantation.

By day 28 after injection, nanowired hPSC-CM spheroids showed indications of functional integration with host myocardium. Nanowired hPSC-CM spheroids had shifted from their original spherical shape at day 1 to an elongated structure on day 28 (Fig. 2L). Nanowired hPSC-CM spheroids formed electrical and mechanical cellular junctions with host myocardium as evidenced by graft-host connexin-43 (Cx-43) (Fig. 2M) and N-cadherin (Fig. 2N) staining, respectively. In addition, isolectin-B4 (IB4) staining revealed host invasion of capillary-like lumen structures that contained blood cells within the grafted spheroids at day 28 (Fig. 2O). Together, these results provided evidence that e-SiNW incorporation into nanowired hPSC-CM spheroids improves short-term engraftment, and the nanowired spheroid showed

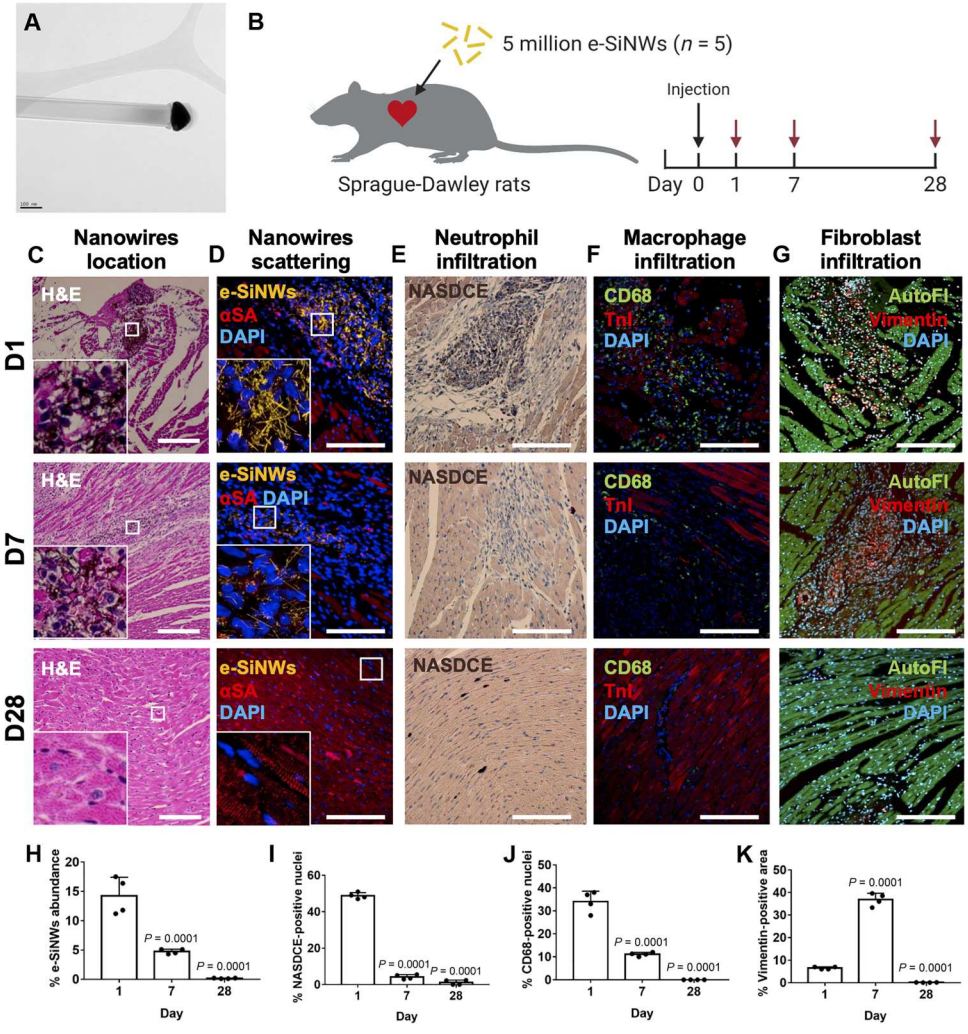

Fig. 1. Biocompatibility of e-SiNWs in rat myocardium. (**A**) Representative transmission electron microscopy image of an n-type e-SiNW used in this study on a carbon grid. (**B**) Experimental outline using 8-to-10-week-old male Sprague-Dawley rats for e-SiNW injection and biocompatibility analysis. Maroon arrows indicate days when analysis was performed. (**C**) Hematoxylin and eosin (H&E) staining of e-SiNW injection site at 1, 7, and 28 days after injection. (**D**) Confocal images of light scattering from injected e-SiNWs in myocardium. (**E**) Neutrophil infiltration identified by naphthol AS-D chloroacetate staining (NASDCE; dark brown). (**F**) Macrophage infiltration identified by CD68 staining. (**G**) Fibroblast infiltration identified by vimentin staining. (**H** to **K**) Quantification of (H) e-SiNWs, (I) neutrophils, (J) macrophages, and (K) fibroblasts at days 1, 7, and 28 after nanowire injection. Data represents means ± SD [n = 3 biologically independent regions from four hearts each, one-way analysis of variance (ANOVA) versus day 1]. Scale bars, 100 nm (A) and 200 μm [(C) to (G)].

long-term electrical, mechanical, and vascular integration with the host myocardium.

Development of nanowired human cardiac organoids for heart repair

Given the biocompatibility of e-SiNWs and the functional engraftment of nanowired hPSC-CM spheroids in healthy adult rat myocardium, we sought to develop an hPSC-based cardiac microtissue platform to treat infarcted hearts. Our laboratory has previously developed human cardiac organoids containing hPSC-CMs, primary hcFBs, human umbilical vein endothelial cells (HUVECs), and human adipose-derived stem cells (hADSCs) as a source of stromal cells (*29*, *38*). Our robust method of producing human cardiac organoids with diverse, yet defined, cell types yielded cardiac microtissues that contained lumenized vascular networks that structurally resemble the vasculature within the developing myocardium. The organoids also supported hPSC-CM contractile development and had fundamental cardiac tissue–level functions that enabled accurate modeling of heart disease and drug cardiotoxicity (*29*, *38*). Motivated by our nanowired hPSC-CM spheroid results, we adapted our biomimetic cardiac organoid platform for cardiac cell therapy by integrating e-SiNWs and evaluating their contractile functions in vitro.

To fabricate nanowired human cardiac organoids, we first constructed nanowired cardiac spheroids containing a 1:1 ratio of e-SiNWs to hPSC-CMs (~1000 hPSC-CMs per spheroid). After 10 days of spheroid culture, supporting cells were seeded onto the preformed nanowired spheroids to form functional nanowired cardiac organoids (Fig. 3A). This sequential seeding approach was inspired by epicardial cell infiltration and mesenchymal diversification

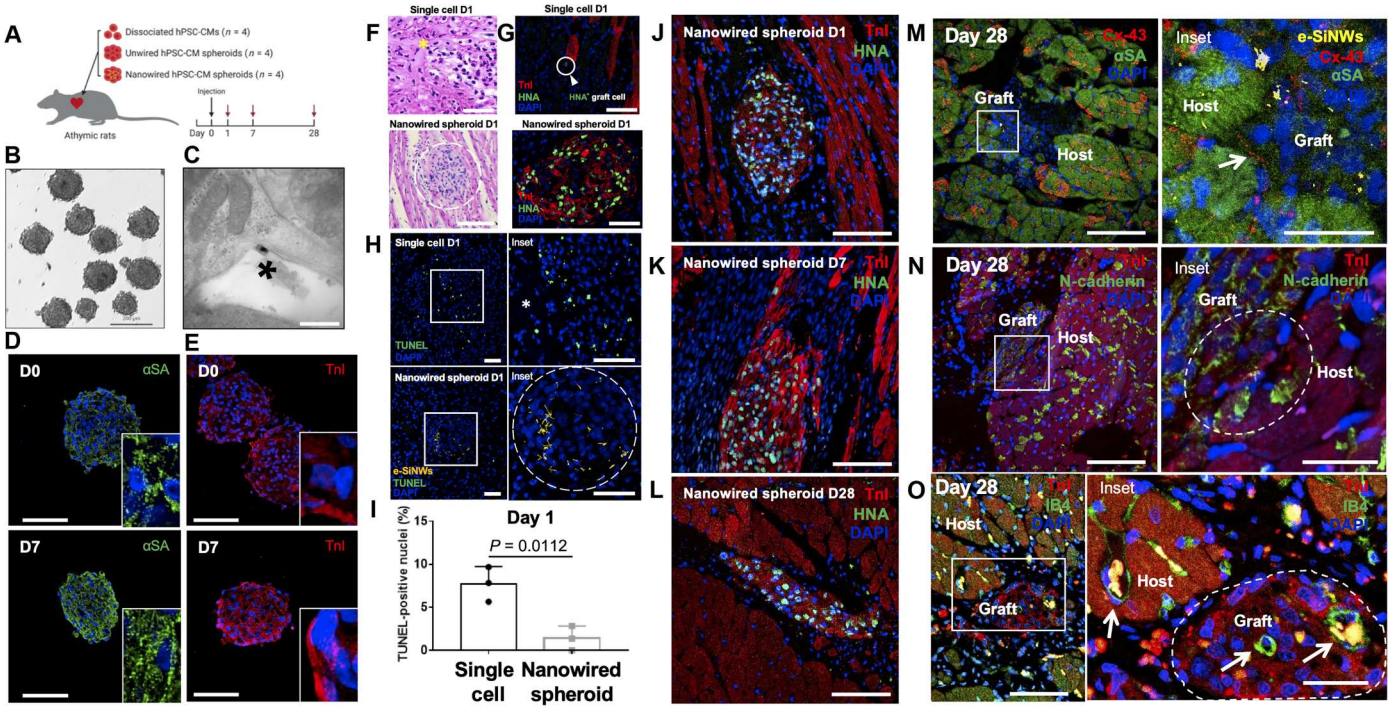

Fig. 2. Nanowired human cardiac spheroid transplantation. (**A**) Experimental outline for intramyocardial injection of hPSC-CM spheroids or nanowired hPSC-CM spheroids. Maroon arrows indicate days when analysis was performed. (**B**) Nanowired hPSC-CM spheroids after 7 days' culture. (**C**) Transmission electron micrograph of e-SiNWs in extracellular space of nanowired spheroids. Asterisk indicates nanowire. (**D** and **E**) Contractile proteins (D) αSA and (E) TnI expressed by nanowired spheroids at days 0 and 7. (**F**) H&E staining of single-cell injection sites (asterisk indicates Matrigel) and nanowired spheroids on day 1. (**G**) TnI and HNA (arrowhead) expression in single cells and nanowired spheroid grafts at day 1. (**H**) TUNEL staining of single-cell injection sites (asterisk indicates Matrigel) and engrafted nanowired spheroids on day 1. (**I**) Ratio of TUNEL-positive cells from sites of single cell or spheroid injection. Data are presented as means ± SD (n = 3 biologically independent grafts, two-tailed Student's t test). (**J** to **L**) Nanowired spheroid grafts in rat myocardium at days 1, 7, and 28. (**M** to **O**) Engraftment of nanowired spheroids at day 28 after transplantation. (M) Connexin-43 (Cx-43) staining of graft-host gap junction formation. (N) N-cadherin staining of mechanical coupling between graft and host myocardium. (O) Isolectin-B4 (IB4) staining of capillary-like structures (arrow) with blood cells within the nanowired spheroid graft. Scale bars, 200 μm (B), 500 nm (C), 100 μm [(D) and (E)], 50 μm [(F), top], 100 μm [(F), bottom], 50 μm (G), 50 μm (H), 100 μm [(J) to (L)], 100 μm [(M) to (O)], and 25 μm (inset).

during postepicardium formation, which produces most of the noncardiomyocyte lineages of the mature heart (fig. S7) (*49*). The organoids self-assembled into compact microtissues approximately 250 μm in diameter (Fig. 3B) and exhibited peripheral organization of hPSC-CMs colocalized with e-SiNWs (Fig. 3, C and D). Vimentin-positive hcFBs and hADSCs located in the interior region of the organoids, with some distributed among hPSC-CMs (Fig. 3, C and E). HUVECs formed capillary-scale lumenized vasculature within the organoids (Fig. 3F and fig. S8). Similar morphological development was observed in unwired cardiac organoids, with hPSC-CMs lining the periphery of the organoid and HUVECs forming lumenized networks (fig. S9).

Since nanowired hPSC-CM spheroids functionally engrafted in healthy myocardium, we next compared the fitness of nanowired cardiac spheroids (100% hPSC-CMs) and organoids (hPSC-CMs + supporting cells) for transplantation into an ischemic environment. We performed an in vitro ischemia challenge on hPSC-CM spheroids and human cardiac organoids (Fig. 3G). We found that nanowired cardiac organoids exhibited significantly less apoptosis than spheroids, as evidenced by a significantly lower presence of TUNEL-positive cells within the cardiac organoids (Fig. 3, H and I). This could be attributed to the nonmyocyte cell population and vascular network within the cardiac organoids providing a more cardioprotective microenvironment to support the survival of hPSC-CMs (*50*). Next, we investigated the effects of e-SiNWs on cardiac organoid synchronization and contractility upon exogenous electrical stimulation (Fig. 3J). When paced at varying frequencies, a greater number of nanowired organoids were able to synchronize consecutively with electrical stimulation compared to unwired organoids (Fig. 3K). Furthermore, nanowired organoids exhibited greater contractility when paced up to 1.5 Hz as evidenced by higher fractional area change during electrical stimulation (Fig. 3L). Therefore, nanowired cardiac organoids are more capable of synchronizing with exogenous electrical pacing and have enhanced contractility compared to unwired cardiac organoids. Only doped e-SiNWs (conductivity, 150 to 500 μS/μm) induced significant improvements in contractility, with undoped SiNWs (conductivity, 0.001 to 0.1 μS/μm) having insignificant effects on contractility across culture (fig. S10), demonstrating that positive nanowire effects are primarily due to conductivity.

Nanowired human cardiac organoids functionally engraft in infarcted myocardium

We used a rat model of myocardial ischemia/reperfusion (I/R) injury to study the effects of unwired and nanowired organoid treatment, as they have been shown to be an effective preclinical animal

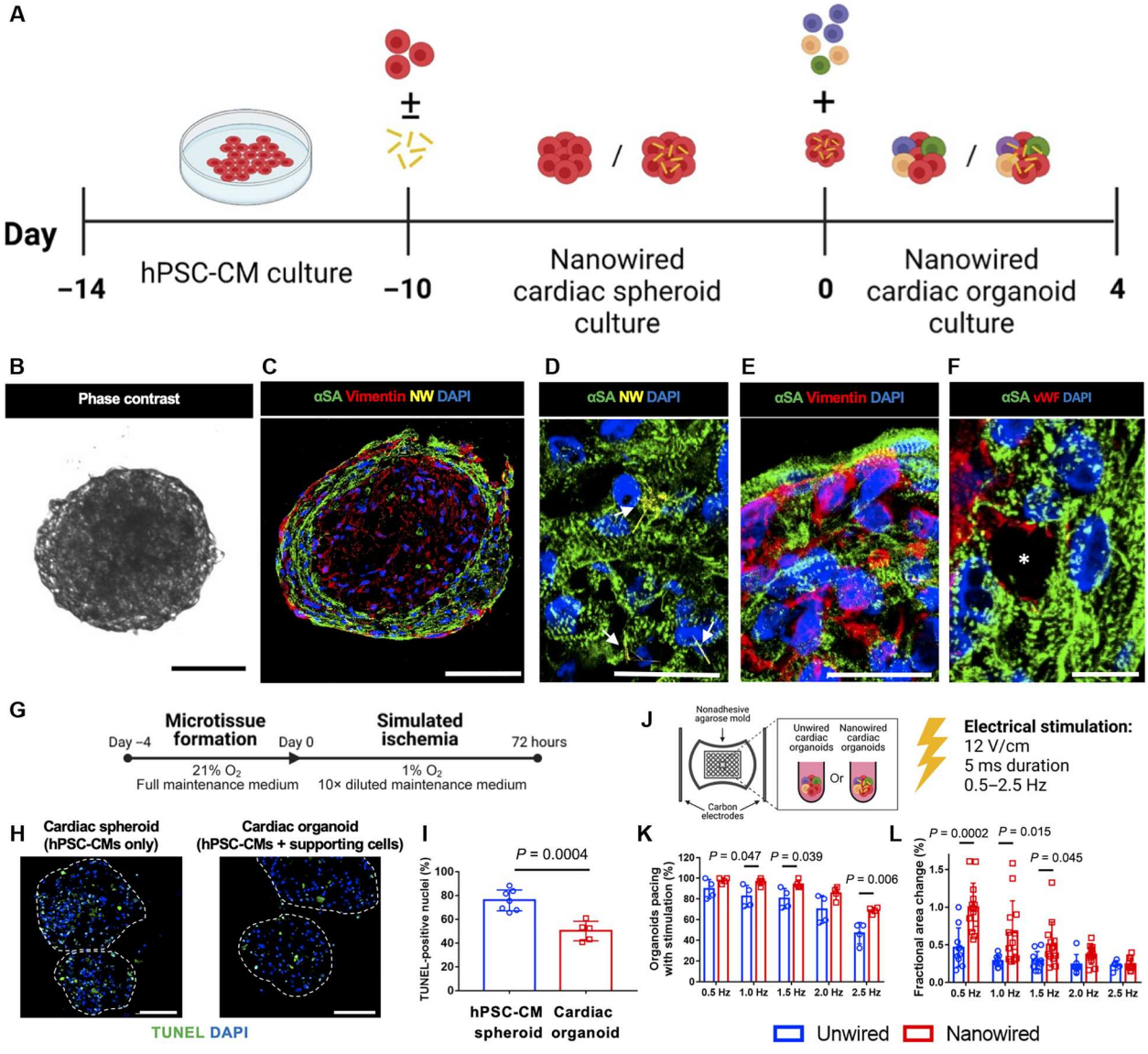

Fig. 3. Nanowired human cardiac organoid development. (**A**) Organoids are prepared by sequential seeding of nonmyocyte supporting cells onto nanowired human cardiac spheroids. (**B**) Representative phase contrast image of nanowired cardiac organoids. (**C**) hPSC-CMs (green) organize on the peripheral region of cardiac organoids. (**D**) Nanowires (NWs) (arrows) are located largely in cardiomyocyte regions. (**E**) Stromal cells are distributed across cardiomyocyte regions and endothelial cells (**F**) form lumen-like structures (*). (**G**) Experimental outline of microtissue survival in simulated ischemia in vitro. (**H**) TUNEL-positive cells with hPSC-CM spheroids and cardiac organoids after 72 hours of simulated ischemia. (**I**) Quantification of the ratio of TUNEL-positive nuclei within spheroids or organoids. Data are presented as means ± SD (n = 5 to 7 biologically independent samples). A two-tailed Student's t test was used for comparing cardiac spheroids and organoids. (**J**) Experimental outline of electrical stimulation of unwired and nanowired organoids at various frequencies. (**K**) Percentage of unwired and nanowired organoids keeping pace with electrical stimulation at various frequencies. Data are presented as means ± SD (n = 4 biologically independent samples). A two-tailed Student's t test was used for comparing cardiac spheroids and organoids at each frequency. (**L**) Fractional area changes of unwired and nanowired organoids at various frequencies. Data are presented as means ± SD (n = 10 biologically independent samples). Two-tailed Student's t test was used for comparing cardiac spheroids and organoids at each frequency. Scale bars, 100 μm [(B) and (C)], 25 μm [(D) and (E)], 10 μm (F), and 100 μm (H).

model for hPSC-CM–mediated heart repair (fig. S11) (*47*, *51*). Two days after cardiac organoid transplantation, we routinely identified grafts in the infarct region, adjacent to necrotic tissue (Fig. 4A). At day 7 after transplantation, both unwired and nanowired organoid grafts were perfused with red blood cell–containing host vasculature (Fig. 4, B and C). Accordingly, we observed a comparable retention rate for both unwired and nanowired organoids (~30%) after normalizing the number of retained grafts at 7 days after transplantation to the number of grafts at 1 day after transplantation (Fig. 4D). This is a higher retention rate compared to other studies using intramyocardial injection of dissociated hPSC-CMs into infarcted rat hearts, which observed <1 to 10% retention by day 7 (*52*).

At 28 days after transplantation, grafted organoids were found mainly within fibrotic regions of the infarct zone (Fig. 4E). Both unwired and nanowired grafts were found to be surrounded by scar tissue (Fig. 4, F and G). Notably, we found nanowired organoid

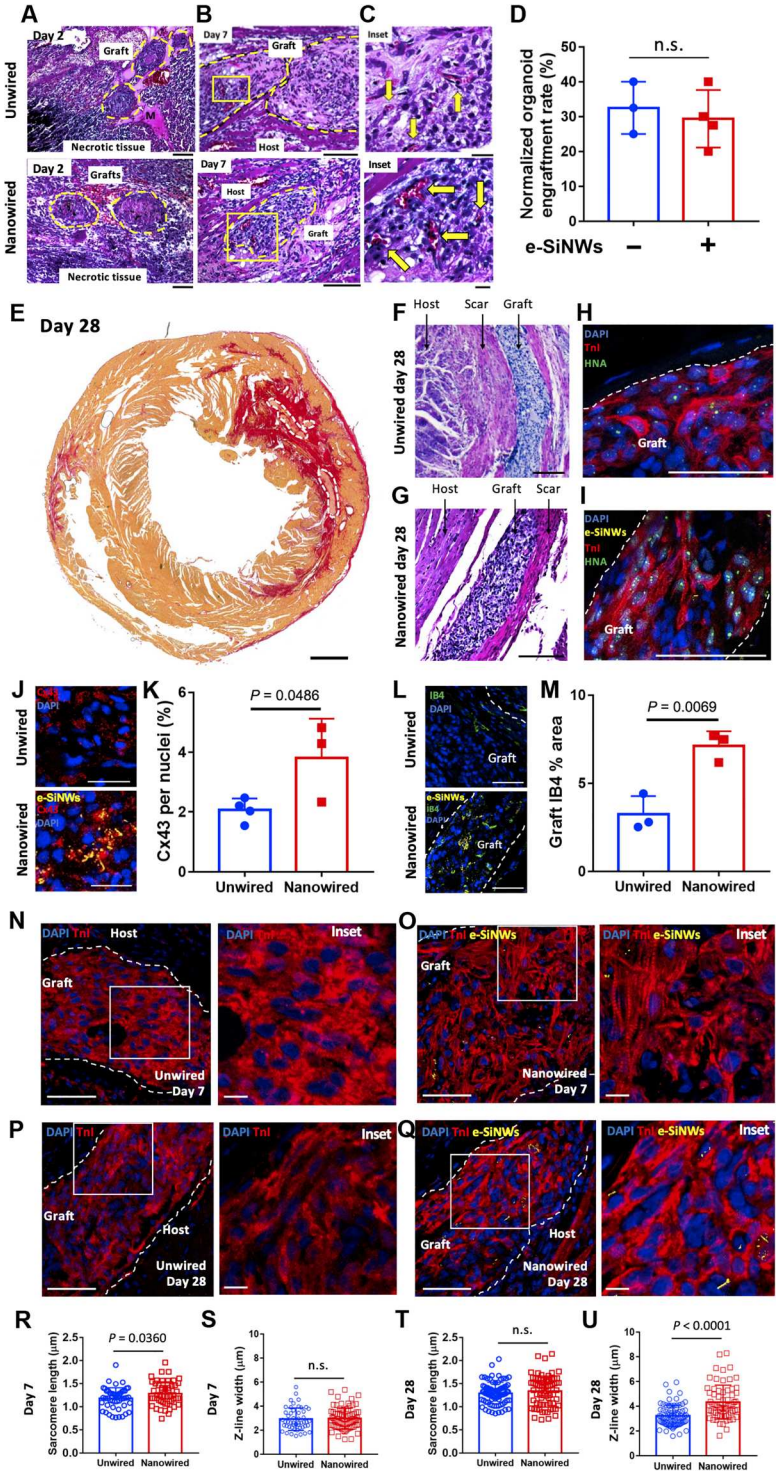

Fig. 4. Nanowired human cardiac organoid transplantation in infarcted rat hearts. (**A**) Organoids grafts near necrotic tissue at day 2. (**B** and **C**) Perfused vasculature within organoid grafts at day 7. (**D**) Ratio of grafts in injured hearts at day 7 normalized to grafts in healthy hearts 1 day after transplantation. $n = 3$ to 4 rats, two-tailed Student's t test. n.s., not significant. (**E**) Grafted organoids (arrows) within fibrotic scar tissue of the left ventricle. yellow, muscle fibers/cytoplasm; red, collagen. (**F**) H&E stain of a graft bordered by fibrotic tissue in unwired organoid–treated rats. (**G**) H&E stain of graft bordered by fibrotic tissue in nanowired organoid–treated rats. (**H** and **I**) TnI expression in unwired (H) and nanowired (I) organoid grafts identified by HNA. (**J** and **K**) Cx-43 in day 28 grafts. (**L** and **M**) IB4-positive vascularization in day 28 grafts. n = average of three biologically independent grafts from three to four rats. (**N** and **O**) TnI expression in (N) unwired and (O) nanowired grafts at day 7. (**P** and **Q**) TnI expression in (P) unwired and (Q) nanowired grafts at day 28. (**R**) Sarcomere length of grafts at day 7. (**S**) Z-line width of grafts at day 7. (**T**) Sarcomere length of grafts at day 28. (**U**) Z-line width of grafts at day 28. $n \geq 40$ biologically independent measurements across three to four grafts from at three to four rats, two-tailed Student's t test. All data represents means ± SD [(R) to (U)]. Scale bars, 100 μm (A), 100 μm (B), 20 μm (C), 1 mm (E), 100 μm [(F) and (G)], 50 μm [(N) to (Q)], and 10 μm (inset).

grafts directly adjacent to necrotic tissue at day 28, indicating their capacity to survive in the most hostile regions of the infarcted myocardium (fig. S12). Unwired and nanowired grafts expressed contractile protein TnI, as shown in HNA-positive regions (Fig. 4, H and I). Compared to in vitro, hPSC-CMs were significantly more aligned in both unwired and nanowired organoid grafts in vivo (fig. S13), confirming progression of their contractile development after transplantation. Nanowired organoid grafts expressed significantly more Cx-43 at day 28 than unwired organoid grafts (Fig. 4, J and K), indicating enhanced long-term retention of electrical coupling within grafts mediated by e-SiNWs. However, we did not observe Cx-43 coupling between the graft and host cardiomyocytes, likely due to the location of grafts within fibrotic tissue in the infarcted hearts. The lack of contacts between engrafted hPSC-CMs

and host myocardium has been a common observation in previous studies (*10*, *53*). Functional electrical coupling between engrafted hPSC-CMs and injured host myocardium has been demonstrated without host-graft Cx-43 junction (*12*). Supporting their long-term engraftment, nanowired grafts had significantly greater abundance of IB4-positive host vessels at day 28 (Fig. 4, L and M), although graft-host anastomosis was not observed within unwired or nanowired organoid grafts at day 7 or 28.

Nanowired human cardiac organoids accelerate in vivo contractile development of transplanted hPSC-CMs

Given the capacity of e-SiNWs to improve the electrical pacing and contractility of cardiac organoids in vitro, we assessed the effects of e-SiNWs on in vivo hPSC-CM contractile development in cardiac organoids. To accomplish this, we compared sarcomere length and z-band width between unwired and nanowired cardiac organoids after 7 and 28 days after transplantation (Fig. 4, N to U). Grafted hPSC-CMs from nanowired organoids had significantly greater sarcomere length at day 7 (~1.3 μm) compared to unwired organoids (~1.2 μm) (Fig. 4R). We identified a trend with an increased z-line width (~4 μm) in nanowired organoid grafts compared to unwired organoid grafts (~3 μm), although not statistically significant (Fig. 4S). By day 28, sarcomere length was comparable between grafted hPSC-CMs from unwired (~1.3 μm) and nanowired organoids (~1.5 μm) (Fig. 4T). However, z-line width was significantly greater at day 28 in nanowired organoids (~5 μm) compared to unwired organoids (~3.5 μm) (Fig. 4U). These results indicate that incorporating e-SiNWs in cardiac organoids accelerates in vivo hPSC-CM sarcomere development in the short term (7 days) and continues to improve contractile structure organization in long-term engraftment (28 days).

Nanowired human cardiac organoid transplantation augments functional recovery from I/R injury in adult rats

To determine the effects of e-SiNW incorporation on cardiac organoid–mediated functional recovery in the host heart, an investigator to whom rat treatment was not disclosed performed and interpreted cardiac echocardiography on all animals before I/R injury (pre-I/R), 24 hours after I/R injury (post-I/R), and 7 and 28 days after injection (Fig. 5A). We established an inclusion criteria of <30% FS post-I/R to ensure consistency among groups. After 4 days of recovery, animals received either no additional surgical procedure (control, $n = 5$), intramyocardial injection of unwired cardiac organoids (unwired, $n = 5$, 500 organoids per rat), or nanowired cardiac organoids (nanowired, $n = 6$, 500 organoids per rat). All groups experienced a severe decline in LV function post-I/R and had comparable post-I/R FS values, indicating effective randomization and similar functional impairment among groups before treatment (Fig. 5, B and C, and table S2). Compared to post-I/R values, control and unwired organoid–treated animals exhibited insignificant recovery of FS at day 7 (Fig. 5B and table S2). Meanwhile, rats treated with nanowired organoids had significantly higher FS at day 7 than post-I/R (Fig. 5B). Accordingly, only rats treated with nanowired organoids had significantly higher FS (Fig. 5C and table S2), FS increase over the post-I/R value (Fig. 5D and table S2), and FS recovery from I/R injury compared to control at day 7 (Fig. 5E and table S2). The ~60% FS recovery at 7 days after transplantation from nanowired organoid treatment (Fig. 5E) demonstrated rapid and effective functional recovery, consistent with our findings of accelerated contractile development in nanowired organoids at day 7 (Fig. 4, Q and R).

On day 28, control rats exhibited insignificant recovery of FS compared to post-I/R, while FS in both unwired and nanowired organoid–treated rats significantly improved (Fig. 5B and table S2). The nanowired organoids significantly improved functional recovery compared to unwired organoids at day 28, as evidenced by significantly higher average FS (Fig. 5C and table S2), FS increase over the post-I/R value (Fig. 5D and table S2), and FS recovery from I/R injury (Fig. 5E and table S2). These results showed that cardiac organoid transplantation is therapeutically efficacious in treating I/R injury in adult hearts and that the incorporation of e-SiNWs provides a synergistic therapeutic benefit to enable superior short-term and long-term improvements in cardiac function.

We used echocardiography to quantify changes in LV dimensions after cardiac organoid transplantation, using pre-I/R values as a benchmark. We observed an increase in LV end-diastolic diameter (LVEDD) when compared to pre-I/R values for control, unwired, and nanowired organoid treated rats at days 7 and 28 (Fig. 5F and table S2). There was no significant difference in average LVEDD values among the groups at any time point (Fig. 5G and table S2). When comparing LVEDD values at day 28 with pre-I/R values, nanowired organoid–treated rats exhibited a significantly lower change compared to control (Fig. 5H and table S2). This showed that 28 days after injury, nanowired organoid treatment promoted the closest return to normal LVEDD relative to unwired organoid treatment and control. For LV end-systolic diameter (LVESD), unwired and nanowired organoid–treated rats had lower LVESD on average at days 7 and 28 compared to control; however, only the nanowired group reached statistical significance (Fig. 5, I and J, and table S2). Similar to the LVEDD results, the change in LVESD at day 28 compared to pre-I/R values was significantly lower only in nanowired organoid–treated rats, indicating the closest return to near-normal LVESD relative to unwired organoid treatment and no treatment (Fig. 5K and table S2). Accordingly, LV wall motion was severely reduced in control rats at day 28 after transplantation (Fig. 5L) but retained greater motion in unwired groups (Fig. 5M) and even greater motion in nanowired groups (Fig. 5N). Together, e-SiNW incorporation significantly augments the therapeutic efficacy of human cardiac microtissue transplantation, primarily by enhancing systolic function and LV remodeling.

Nanowired human cardiac organoid transplantation mitigates maladaptive remodeling post-I/R

Pathological ventricular remodeling after myocardial infarction, including cardiac fibrosis, LV wall thinning, and cardiomyocyte hypertrophy, is associated with a significantly increased risk of heart failure (*54*). Therefore, we assessed the effects of nanowired cardiac organoid transplantation on LV remodeling by evaluating cardiac fibrosis and LV infarct wall thickness at day 28 after treatment. Using picrosirius red staining, we observed I/R injury–induced collagenous scar tissue in the LV wall of all experimental groups (Fig. 6A). However, we found that the global ratio of fibrotic tissue occupying the LV wall was significantly reduced in both unwired and nanowired organoid–treated hearts compared to control (Fig. 6B) and local fibrosis in the infarct zone (Fig. 6C). Fibrosis results were confirmed using a quantitative assay of hydrolyzed sections of infarcted myocardium (Fig. 6D). Both unwired

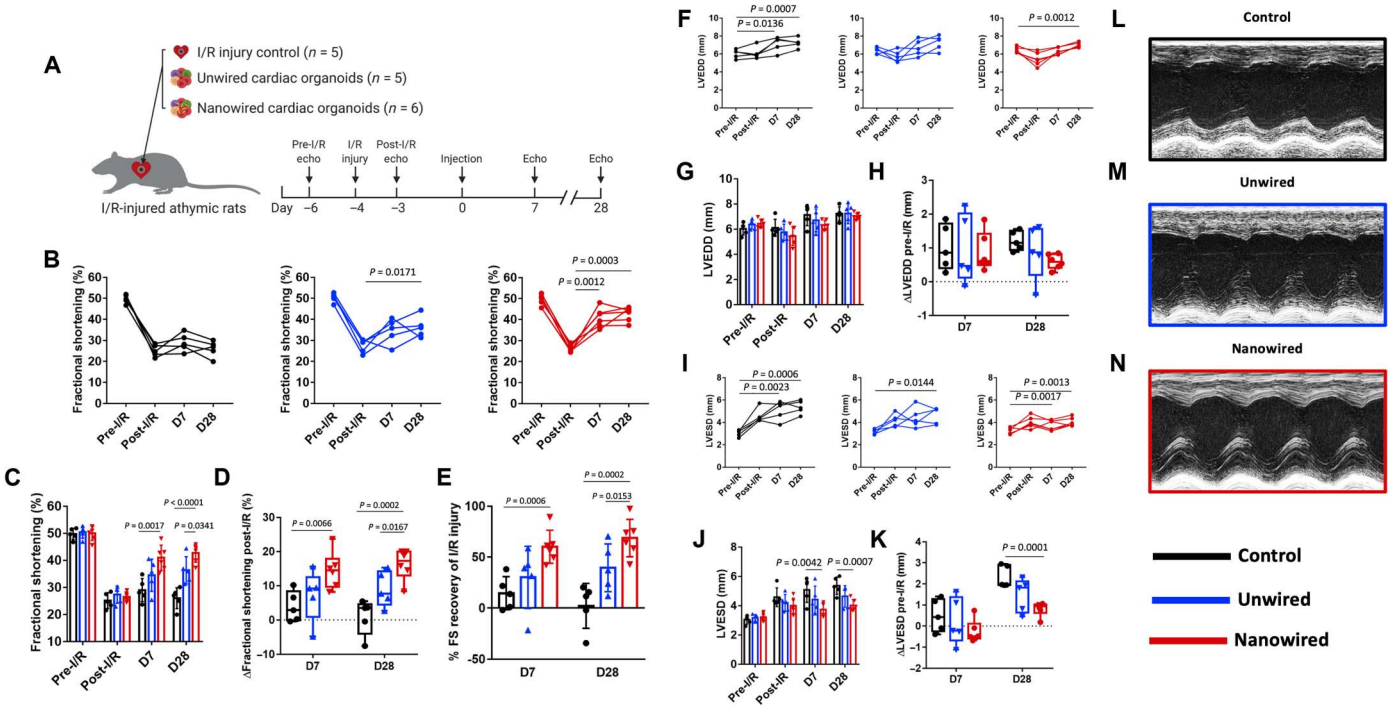

Fig. 5. Functional recovery after nanowired human cardiac organoid transplantation. (**A**) Experimental outline of cardiac organoid transplantation in I/R-injured rat hearts. (**B**) FS of each rat at pre-I/R, post-I/R, and 7 and 28 days after transplantation. (n = 5, 5, and 6 rats for control, unwired, and nanowired treatment groups, respectively). Paired two-tailed Student's t test. (**C**) Average FS values at each time point. (**D**) Average percent change in FS at days 7 and 28 compared to post-I/R. (**E**) Average percent recovery of FS lost to I/R injury at days 7 and 28. One-tailed Student's t test. (**F** and **G**) LVEDD of each rat at pre-I/R, post-I/R, and 7 and 28 days after transplantation. Paired two-tailed Student's t test. (G) Average LVEDD values at each time point for each treatment group. (**H**) Average change in LVEDD at days 7 and 28 compared to pre-I/R. One-tailed Student's t test. (**I**) LVESD of each rat at pre-I/R, post-I/R, and 7 and 28 days after transplantation. Paired two-tailed Student's t test. (**J**) Average LVESD values at each time point. (**K**) Average change in LVESD at days 7 and 28 compared to pre-I/R. One-tailed Student's t test. (**L** to **N**) Representative M-mode echocardiographs at day 28 for control (L), unwired (M), and nanowired (N) groups. [(B) to (K)] Data represents means ± SD. A Bonferroni-corrected $P < 0.025$ was used to determine statistical significance.

and nanowired organoids significantly reduced total collagen content in infarcted hearts at day 28, with nanowired organoids having the greatest reduction of collagen content (Fig. 6D). Furthermore, we found that unwired and nanowired organoid–treated hearts had significantly less LV wall thinning at the infarct site than control (Fig. 6E), which agreed with our findings of improved systolic function. Nanowired organoids elicited significantly greater arteriole density at the infarct site (Fig. 6, F and G). Thus, nanowired cardiac organoid transplantation significantly reduced cardiac fibrosis and LV wall thinning and promoted therapeutic angiogenesis post-I/R.

To further assess the effects of nanowired organoid transplantation on LV remodeling, we investigated the extent of cardiac hypertrophy in border and remote zones from base to apex of the host LV after 28 days after transplantation (Fig. 6H and fig. S14A). Wheat germ agglutinin (WGA) staining enabled visualization of host cardiomyocyte size in remote and border zones of rat hearts (Fig. 6I and fig. S14B). Compared to control, the cross-sectional area of host cardiomyocytes in the border zone was significantly lower in nanowired organoid–treated hearts (Fig. 6J). In the remote zone, cardiomyocytes in both the unwired and nanowired organoid–treated hearts were significantly smaller than control hearts (Fig. 6J). These results indicate that cardiac organoid transplantation mitigated compensatory hypertrophy in I/R-injured myocardium. This observation supports the improvement of systolic function and preservation of LVEDD and LVESD observed via echocardiography in nanowired organoid–treated rat hearts (Fig. 5). Therefore, the incorporation of e-SiNWs in cardiac organoids provided synergistic therapeutic benefits in preventing maladaptive ventricular remodeling, which agrees with the additive effect observed in functional recovery.

Nanowired cardiac organoids promote regenerative macrophage polarization in the graft and border zone following I/R injury

We have demonstrated that intramyocardial injection of bare e-SiNWs does not elicit chronic inflammation in healthy myocardium (Fig. 1). After myocardial infarction, inflammation plays a central role in the adaptive remodeling process to prevent early mortality. Macrophages, especially, are involved in every stage of the inflammatory process after myocardial infarction (*55*). Therefore, we investigated the effects of nanowired organoid transplantation on macrophage infiltration in grafted organoids and the border zone in the host heart. We did not observe chronic inflammation associated with organoid grafts and found no significant difference between the percent area coverage by CD68-positive cells in unwired and nanowired grafts at days 7 and 28 after transplantation (fig. S15, A and B). Macrophage infiltration in the grafts decreased

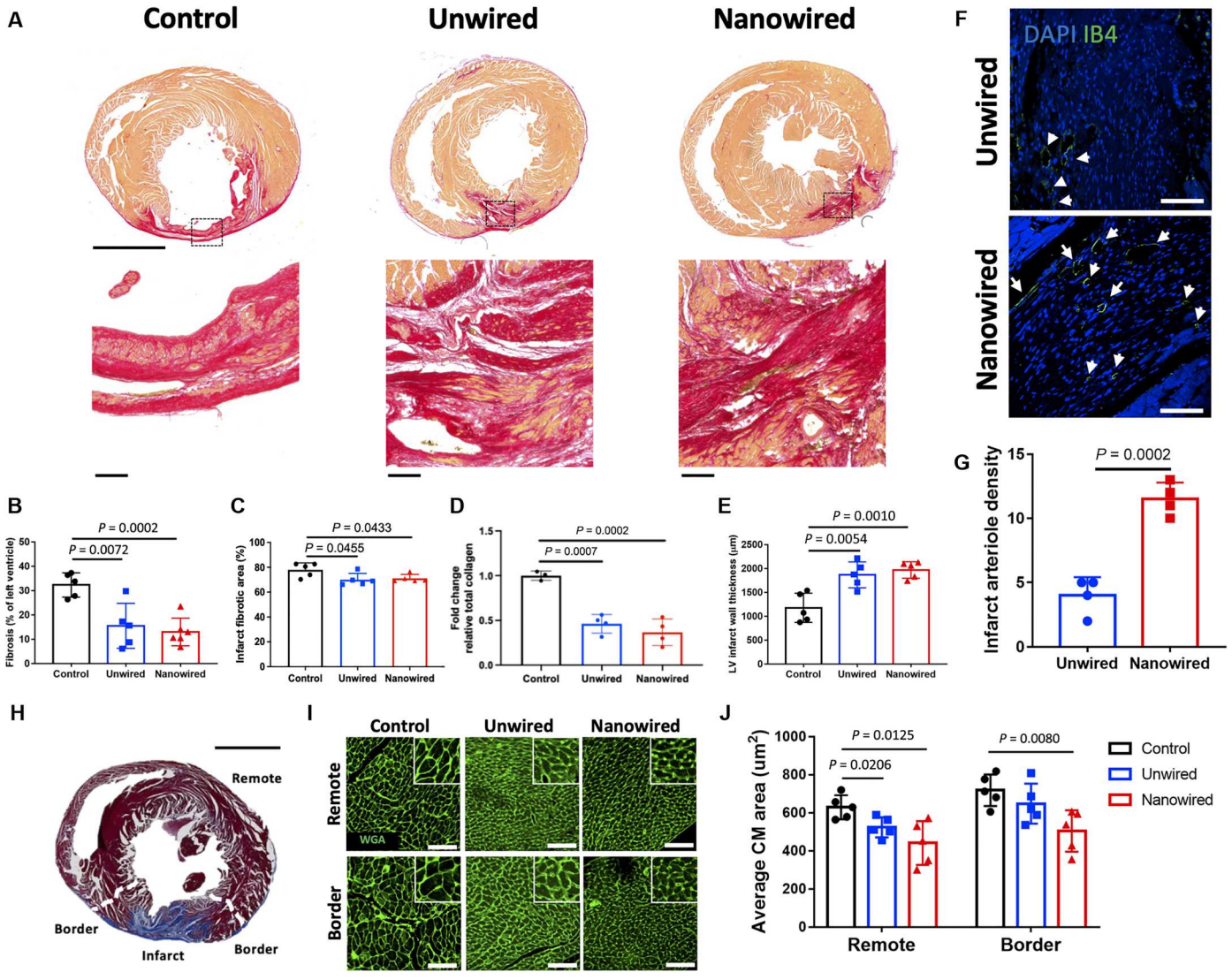

Fig. 6. Attenuation of maladaptive LV remodeling after nanowired human cardiac organoid transplantation. (**A**) Representative picrosirius red stains of infarcted rat hearts (red, collagen I/III; yellow, myofibers). Scale bars, 3 mm (top) and 200 μm (bottom inset). (**B**) Average percent global fibrosis of left ventricle at day 28. (**C**) Average percent local fibrosis of infarct at day 28. *n* = average of three sections base to apex from four to five hearts each group, two-tailed Student's *t* test. (**D**) Total collagen (hydroxyproline) quantification in infarcted myocardium. *n* = 3 to 4 rats, one-way ANOVA. (**E**) Average LV wall thickness at day 28. (**F**) Arterioles (10 to 100 μm in diameter) in the infarct zone at day 28. (**G**) Average infarct arteriole density in hearts treated with unwired or nanowired organoids. (*n* = average of three sections base to apex from four to five hearts each group, two-tailed Student's *t* test). (**H**) Representative Masson's trichrome staining of the fibrotic infarct zone, adjacent border zone, and remote regions the host heart. (**I**) Representative images of wheat germ agglutinin (WGA)–stained host cardiomyocytes in the border and remote zones of the heart at day 28 with magnified images of cell borders (top right corner). Scale bars, 100 μm. (**J**) Average cross-sectional area of host cardiomyocytes in the border and remote regions of the host heart. (*n* = average of three regions each from base to apex in each of five hearts per condition, two-tailed Student's *t* test). All data represent means ± SD.

substantially from days 7 to 28 (fig. S15B). In addition, organoids with or without nanowires did not exacerbate macrophage presence in the border zone of the host heart (fig. S15, C and D). We further analyzed macrophage phenotype in organoid grafts and the host heart border zone to determine proinflammatory and proregenerative macrophage responses to cardiac organoids (*55*). Nanowired grafts had a significantly greater ratio of proregenerative (CD206-positive) macrophages at day 7 compared to unwired grafts (fig. S16, A and B). However, the difference was not significant at day 28 (fig. S16B). Nanowired cardiac organoid treatment resulted in significantly less proinflammatory CD86-positive macrophages in the border zone of the infarcted heart at day 28 compared to control (fig. S16, C and D). Furthermore, there was a significantly greater ratio of proregenerative CD206-positive to CD86-positive macrophages in the border zone in the nanowired organoid treatment compared to both control and unwired (fig. S16E). Together, these results support the high cardiac biocompatibility of the e-SiNWs. Further, they indicate that nanowired cardiac organoids induce a more proregenerative macrophage phenotype in the graft and the border zone, supporting the improved functional recovery at days 7 and 28 (Fig. 5).

DISCUSSION

While hPSC-CMs have been shown to restore the contractile functions of infarcted hearts in various animal models, the conventional strategy has primarily involved intramyocardial injection of a large quantity of dissociated hPSC-CMs (e.g., 10×10^6 hPSC-CMs per rat) to replace cardiomyocytes lost after injury. These approaches have been limited by low cell retention and survival, moderate functional improvement, arrhythmogenic risk, and poor scalability (*10*, *15*–*18*, *53*, *56*–*58*). To address these limitations, we developed a powerful human cardiac cell therapy platform by incorporating biodegradable and biocompatible e-SiNWs into human cardiac microtissues to augment their therapeutic efficacy, resulting in the first demonstration of heart repair by human cardiac organoids synergized with conductive nanomaterials.

We found that e-SiNWs are biocompatible, in agreement with previous reports (*42*, *59*), and they did not exacerbate the inflammatory response in healthy or disease settings. Nanowired hPSC-CM spheroids improved hPSC-CM survival and contractile development after intramyocardial injection compared to dissociated hPSC-CMs. We further developed injectable nanowired cardiac organoids by combining e-SiNWs, hPSC-CMs, and supporting cells in a bioinspired fabrication method, which improved ischemia tolerance of cardiac microtissues compared to hPSC-CM spheroids. Compared to unwired cardiac organoids, nanowired organoids significantly improved electrical pacing and contractility of cardiac microtissues in vitro. Correspondingly, nanowired cardiac organoids significantly improved cardiac function, mitigated maladaptive LV remodeling, and accelerated contractile development of grafted hPSC-CMs in infarcted rat hearts compared to unwired organoids after intramyocardial injection. While unwired cardiac organoids are therapeutically efficacious, e-SiNW incorporation provides a distinct synergistic therapeutic benefit to augment hPSC-CM–mediated heart repair, including greater graft vascularization and infarct arteriole density one month after transplantation.

Compared to recent studies that injected 10×10^6 dissociated hPSC-CMs per rat using the same injury model (*51*, *60*), nanowired human cardiac organoids achieved superior functional recovery with more than an order of magnitude fewer cells (~0.5×10^6 hPSC-CMs per rat). Specifically, the previous studies reported ~8% FS improvement 1 month after transplantation of 10×10^6 dissociated hPSC-CMs per rat (*51*, *60*), yet we achieved ~9% improvement in FS using unwired organoids and ~16% FS improvement with nanowired organoids. When normalized to the FS loss (~23%) caused by the I/R injury, we achieved ~39% FS recovery with unwired organoids and ~ 69% FS recovery with the nanowired organoids at day 28. While our observed engraftment size was smaller than some previous reports, there is no clear relationship between graft size and cardiac repair, as previous studies have reported insignificant contractile functional recovery even with >1 mm^2 hPSC-CM engraftments (*56*). Further studies into the gene expression of infarcted host myocardium and engrafted organoids will be important for mechanistic insight on the nanowired cardiac organoid mediated cardiac repair.

One limitation of our study is the sample size (n = 5 to 6). A greater sample size would increase the confidence of multiple comparisons in future studies. While significant differences in scale and electrophysiology between human and rodent hearts (high resting heart rates, different ion channel expression, and current densities) limits the study of graft-associated arrhythmic events in rats in our present study (*61*, *62*), experimental and computational evidence shows that arrhythmogenic risks of cell therapy are dependent on the number of engrafted cells (*63*–*65*). Therefore, achieving maximal therapeutic efficacy with a minimized dose of hPSC-CMs enabled by conductive nanomaterials and human cardiac organoids represents a transformative strategy for clinical translation of hPSC-CM therapy. Future work will investigate the arrhythmogenicity of nanowired human cardiac organoids with optical mapping in a large animal porcine model. While nanowires have been explored for various translational applications (e.g., wound healing) (*66*), conductive nanowires have been demonstrated with remarkable capacity to improve therapeutic efficacy of implanted hPSC-CMs.

In summary, nanowired human cardiac organoids significantly augment the therapeutic potential of hPSC-CMs for heart repair. While cardiac organoids have been used for cardiac tissue engineering applications, this study reveals e-SiNWs as a class of biocompatible, conductive nanomaterials that facilitate contractile and noncontractile benefits in hPSC-CM transplantation. Given the emerging clinical applications of hPSC-CMs to treat infarcted hearts, these results have direct translational impacts for conductive nanomaterials in cardiac cell therapy and implications in other conductive tissues (e.g., skeletal muscle and neuronal tissues).

MATERIALS AND METHODS

Cell culture

Following procedures previously described in (*67*), hPSC-CMs (iCell Cardiomyocytes, FUJIFILM Cellular Dynamics Inc., Madison, WI, USA) were cultured according to the manufacturer's protocol. Briefly, hPSC-CMs were plated on 0.1% gelatin-coated six-well plates in iCell Cardiomyocyte plating medium (FUJIFILM Cellular Dynamics Inc.) at a density of about 3×10^5 to 4×10^5 cells per well and incubated at 37°C in 5% CO_2 for 4 days. Two days after plating, the plating medium was removed and replaced with 4 ml of iCell Cardiomyocytes maintenance medium (FUJIFILM Cellular Dynamics Inc.). After 4 days of monolayer preculture, cells were detached using trypLE Express (Gibco Life Technologies, Grand Island, NY) and prepared for organoid fabrication. hcFBs (Lonza, Basel, Switzerland) were cultured in fibroblast growth medium 3 medium (PromoCell, Heidelberg, Germany) and used at passages 3 to 4 for organoid fabrication. HUVECs (Lonza) were cultured in endothelial growth medium 2 medium (PromoCell) and used at passages 2 to 3 for organoid fabrication. hADSCs (Lonza) were cultured in ADSC growth medium (Lonza) and used at passages 3 to 4 for organoid fabrication. Cells tested negative for mycoplasma contamination according to the vendor. Culture medium for cardiac organoids was composed of a ratiometric combination of cell-specific medium reflecting the cell ratio of the organoid. In organoid medium, hPSC-CM maintenance medium (supplied without glucose) was substituted with glucose-containing F12/Dulbecco's modified Eagle's medium (DMEM) with 10% fetal bovine serum, 1% glutamine, and 1% non–essential amino acids (Gibco).

Fabrication of nanowired hPSC-CM spheroids

Cardiac spheroids were fabricated according to our previously published methods (*44*, *67*). Briefly, agarose hydrogel micromolds were prepared using 2% agarose (Sigma-Aldrich, St. Louis, MO) with

master micromolds from Microtissues Inc. (Providence, RI). The agarose molds contained 35 microwells with hemispheric bottoms (800 μm in diameter and 800 μm in depth) to facilitate the formation of spherical microtissues. A solution containing a 1:1 ratio of e-SiNWs to hPSC-CMs was dispensed into each mold to fabricate nanowired spheroids containing around 1000 hPSC-CMs and 1000 n-type e-SiNWs (diameter ≈ 100 nm, length ≈ 10 μm, and Si/P = 500) per spheroid. The doping ratio was chosen to obtain a high conductivity (150 to 500 μS/μm) compared to cell culture medium (~1.75 μS/μm) and myocardium (~0.1 μS/μm) to create highly electrically conductive microenvironments within the spheroids. The unwired hPSC cardiac spheroids were fabricated using the same method without adding e-SiNWs.

Fabrication of nanowired human cardiac organoids

Details of human cardiac organoid fabrication were described in our previous publications (*38*, *68*). To fabricate sequentially seeded cardiac organoids, we first fabricated nanowired cardiac spheroids as described in the previous section. After 10 days of nanowired spheroid culture, the supporting cell mixture was seeded onto the molds after careful aspiration of the spheroid medium, with a targeted ratio of 55% hPSC-CMs, 24% hcFBs, 14% HUVECs, and 7% hADSCs. After an additional 4 days of organoid culture, cardiac organoids were prepared for injection.

Simulated ischemia and assessment of apoptosis

Ischemic conditions were simulated as previously described (*69*). Briefly, ischemic medium, which was produced via 10-fold dilution of organoid maintenance medium with glucose-free/serum-free medium (glucose-free DMEM, Gibco), was added to hPSC-CM spheroid or cardiac organoid cultures before they were placed in a hypoxia chamber (ProOx Model 110, BioSpherix, Parish, NY) set at 1% O_2 for 24 hours. The ischemia-challenged microtissues were flash-frozen in Tissue-Tek OCT compound (Sakura, Torrance, CA) and cryosectioned, fixed in 4% paraformaldehyde solution for 10 min, then washed in PBS for 30 min. After PBS washes, sections were incubated in permeabilization solution (0.1% Triton X-100 and 0.1% sodium citrate in PBS) for 2 min on ice. Then, 50 μl of TUNEL reaction mixture (Sigma-Aldrich) was added to the samples and incubated in 37°C for 1 hour. After washing in phosphate-buffered saline with 0.1% Triton X-100 (PBST) (three times at 5 min), nuclei were counterstained with 4′,6-diamidino-2-phenylindole (DAPI) (Molecular Probes/Invitrogen, Eugene, OR) for 15 min at ambient temperature. Following the final wash procedure (PBS, three times at 5 min), glass coverslips were added to the slides using Fluoro-Gel (Electron Microscopy Sciences, Hatfield, PA). A TCS SP5 AOBS laser scanning confocal microscope (Leica Microsystems) was used for imaging the stained microtissue sections.

Electrical stimulation of cardiac organoids

Following previously published methods (*67*), microtissue pacing was conducted via electrical stimulation (C-Pace unit, Ion Optix, Milton, MA, USA) of organoids in the agarose molds suspended in culture medium. Organoids were stimulated (12 V/cm, 5 ms) over a range of frequencies (0.5 to 2.5 Hz), and they were observed under bright-field microscopy and video-recorded with a Carl Zeiss Axiovert A1 Inverted Microscope (Zeiss, Göttingen, Germany). The percentage of organoids keeping pace with exogenous stimulation was calculated. In addition, thresholding in ImageJ was used on high-contrast image series from recorded videos and graphed to generate beating profiles and quantify fractional area change. Fractional area change was calculated as the percent change in organoid area between contraction and relaxation.

Video and image analysis of beating microtissues

As we have described previously (*67*), videos of spheroids and organoids were recorded with a Carl Zeiss Axiovert A1 Inverted Microscope using Zen 2011 software (Zeiss, Göttingen, Germany) with capture rate of 14 frames/s. Then, the videos were converted to a sequence of TIFF format pictures by ImageJ [National Institutes of Health (NIH)] (*70*). Threshold edge-detecting in ImageJ was used on high-contrast microtissue pictures and graphed to realize contraction profiles, from which the fractional area change was calculated.

Transmission electron microscopy

As we have described previously (*67*), e-SiNWs were gently sonicated in isopropyl alcohol and dispersed onto lacey carbon grids (Ted Pella Inc.). Transmission electron microscopy imaging was conducted using a 300-kV FEI Tecnai G2 F30 Super Twin transmission electron microscope. Spheroids were fixed with 2.5% glutaraldehyde, postfixed in PBS-buffered 1% osmium tetroxide with 1.5% K+ ferricyanide, dehydrated in graded ethanol and acetonitrile, and embedded in PolyBed 812 (Polysciences). Seventy-nanometer-thick spheroid sections were prepared using a Leica UltraCut R and a diamond knife, stained with Hanaichi Pb citrate and uranyl acetate, and imagined using a JOEL 200 CX transmission electron microscope.

Injection of e-SiNWs and hPSC cardiac spheroids into healthy rat hearts

Following our published methods (*67*), to evaluate the cardiac biocompatibility of e-SiNWs, male Sprague-Dawley rats (8 to 10 weeks old, Charles River) were anesthetized with 3% isoflurane in induction chamber, endotracheally intubated, and mechanically ventilated. A left thoracotomy was performed to expose the heart. The pericardium was opened and 5 million silicon nanowires in 50 μl of PBS were injected into threqe different sites of LV anterior wall using syringes with 31-gauge needles. For hPSC cardiac spheroid injection, male athymic rats (8 to 10 weeks old, RNU Nude rats, Charles River) were anesthetized, intubated, ventilated, and prepared for surgery. A left thoracotomy was performed to expose the heart. The pericardium was opened, and a total of ~30 hPSC cardiac spheroids per rat (i.e., 30×10^3 hPSC-CMs per rat) or 30×10^3 single hPSC-CMs per rat were injected into three different sites (50 μl at each site) of LV anterior wall using 29-gauge needles. Equivalent volumes of Matrigel (20 μl) were used in all transplantation experiments throughout this study as a thermoresponsive biomaterial to occupy the dead volume of the syringe and seal the injection site. The hPSC-CMs and organoids were not suspended in Matrigel but were loaded in the syringe in front of the Matrigel "plug." After injection, the thoracotomy incision was sutured and the animal was recovered for 1 day, 7 days, and 28 days before heart harvest for histological analysis. The influences of the injected e-SiNWs and hPSC cardiac spheroids on the rat cardiac function were examined on days −1, 1, 7, and 28 after injection by ECG and echocardiography as described below. All the surgical procedures and pre-/postoperative care were performed

following NIH guidelines for the care and use of laboratory animal (NIH publication No. 86-23, revised 1996), and they were under the supervision of the Institutional Animal Care and Use Committee of the Medical University of South Carolina (MUSC).

Rat model of I/R injury

Following procedures we have described previously (*67*), male athymic rats (8 to 10 weeks old, RNU Nude rats, Charles River) were anesthetized with isoflurane, intubated, and mechanically ventilated (SomnoSuite Low-Flow Anesthesia System, Kent Scientific). Rodent Surgical Monitor (INDUS instruments) was used to monitor animal′s condition throughout the surgery, including heart rate, body temperature, and heart function through ECG. A left thoracotomy was performed to expose the heart. The pericardium was opened, and the left anterior descending coronary artery was ligated below the left atrial appendage level using a 7-0 Prolene suture (Ethicon). Occlusion was confirmed by LV blanching and ST elevation on ECG after ligation. After 1 hour, the ligation was released, the chest cavity was aseptically closed, and the rat was allowed to recover for 1 day for echocardiographic measurement. For short-term histological analysis (time points up to and including day 7), rats with I/R injuries that caused a measurable decrease in FS were deemed sufficient for injection. For long-term histological analysis (day 28) and functional recovery studies, the rats that met the echocardiographic inclusion criterion (FS < 30%) were selected for experiments and randomly assigned into experimental groups.

Human cardiac organoid injection protocol

We injected organoids 4 days after I/R induction to allow angiogenesis-associated wound healing processes to reach their peak (*10*). The rats that met our inclusion criterion were anesthetized with isoflurane, intubated, and mechanically ventilated. A second thoracotomy was performed to expose the heart. In preparation for injection, one-third of the total number of cardiac organoids was manually loaded into each of the three syringes with a Matrigel plug, which was used to occupy the dead space in the syringe for organoid injection and plug the injection path to prevent washout of organoids. Then, the nanowired or unwired cardiac organoids containing a total of either ~250×10^3 hPSC-CMs per rat (short-term analysis; ≤day 7) or ~500×10^3 hPSC-CMs per rat (long-term analysis; day 28) were injected with a modified 29-gauge needle into the region surrounding the injured area at three sites (50 μl per site). I/R rats without the cell injection were used as controls and did not receive a second surgery. Once the injections were completed, the chest was closed in three layers, and the animal was recovered with buprenorphine administered intraperitoneally to provide pain relief.

Echocardiography

Following procedures we have described previously (*67*), transthoracic echocardiography was performed using Vevo2100 ultrasound imaging system (VisualSonics, Toronto, Canada) with a 13 to 24 MHz linear array transducer (MS250). Rats were placed in supine position on a warming platform at 37°C under light (1 to 2%) isoflurane anesthesia to maintain the heart rate between 350 and 450 beats/min during imaging procedure. Cardiac function was examined using parasternal long-axis and short-axis 2D B-mode images and M-mode images at parasternal short-axis mid-papillary level. Offline image analyses were performed by an experienced investigator blind to the experimental groups using the dedicated Vevo LAB software. FS was calculated by the equation: FS = (LV end-diastolic dimension − LV end-systolic dimension)/LV end-diastolic dimension.

Histological analysis of in vitro cultured microtissues

Following procedures we have described previously (*67*), microtissues (~30 to 35) were flash-frozen in Tissue-Tek OCT compound (Sakura, Torrance, CA) and cryosectioned into 7-μm thickness layers onto glass slides for immunohistochemistry. The frozen sections were fixed with precooled acetone (−20°C) for 10 min. The fixative was poured off and the acetone was left to evaporate from the sections for 5 min at room temperature before immunostaining as described below.

Histological analysis of harvested cardiac tissue

Following procedures we have described previously (*67*), excised rat hearts were fixed overnight in 4% paraformaldehyde solution (Sigma-Aldrich) and then 70% ethanol before paraffin embedding. Using an automated microtome (LeicaRM2255, Leica, Exton, PA), paraffin-embedded hearts were sectioned into 8 μm in thickness. Slides were deparaffinized in xylene for 5 min and rehydrated using an ethanol gradient. Slides were stained with hematoxylin and eosin (H&E), picrosirius red stain kit (Abcam), and Masson′s trichrome stain kit (Sigma-Aldrich) or processed with heat-activated antigen retrieval solution (Vector Laboratories, Burlingame, CA) for immunostaining as detailed below.

Immunostaining

Following our procedures described previously (*67*), fixed microtissues or rat heart sections were washed with PBS, permeabilized with 0.1% Triton X-100 (Sigma-Aldrich) and blocked with 10% bovine serum albumin (Sigma-Aldrich) for 2 hours at room temperature. Primary antibodies were applied overnight, and secondary antibodies were applied for 2 hours at room temperature, with 3× 10-min PBST washes between. All antibody details can be found in table S3, and the antibodies used in this study are as follows: rabbit anti–pan-TnI (Invitrogen, 710580, lot# 1997919), rabbit anti–vimentin (Abcam, ab92547, lot# GR3258719-11), rabbit anti–von Willebrand factor (vWF) (Abcam, ab6994, lot# GR3180938-1), mouse anti-αSA (Abcam, ab52917, lot# GR3174517-4), rabbit anti–Cx-43 (Sigma-Aldrich, C6219), mouse anti-CD31 (BD Biosciences, 550274, lot# 5170510), mouse anti–N-cadherin (BD Biosciences, 610920, lot# 4357631), mouse anti-CD68 (Bio-Rad, MCA1957, lot# 0515), mouse anti–B7-2/CD86 (Novus Biologicals, NBP225208, lot# 942-1P221206), rabbit anti-CD206 (Proteintech, 50-173-2199, lot# 50-173-2199), mouse anti-HNA (Abcam, ab191181, lot# GR3192103-3), goat anti-mouse Alexa Fluor 546 (Invitrogen, A-11030, lot# 2026145), goat anti-rabbit Alexa Fluor 647 (Invitrogen, A32733, lot# 2047630), and isolectin Alexa Fluor 488 conjugate (IB4) (Vector Laboratories, FL-1201-.5, Lot# ZB0406). Nuclei were counterstained with DAPI (Molecular Probes/Invitrogen, Eugene, OR) diluted in PBST for 30 min at ambient temperature. Following the final wash procedure (PBST, three times at 5 min), glass coverslips were added to the slides using Fluoro-Gel (Electron Microscopy Sciences, Hatfield, PA). Last, a TCS SP5 AOBS laser scanning confocal microscope (Leica Microsystems Inc., Exton, PA) was used to acquire fluorescent images. HNA staining was

performed from base to apex every 100 μm to identify grafts in hearts. Sections in the grafts were then stained with specific antibodies.

Total collagen content quantification

Hydroxyproline content from formalin-fixed paraffin-embedded tissue sections was carried out using a colorimetric total collagen assay (BioVendor LLC, QZBTOTCOL1) according to the manufacturer's instructions. Briefly, ten 8 μm tissue sections from infarcted regions were transferred into a tube of 6 M hydrochloric acid and incubated overnight at 95°C to hydrolyze the samples. A portion of the hydrolysate was used to quantify total protein content with a BCA assay (Thermo Fisher Scientific, 23227), while another portion was used in the total collagen assay to quantify hydroxyproline content. Hydroxyproline content was then normalized to total protein content to yield total relative collagen quantification.

Graft contractile development analysis

Single-cell cardiomyocyte analysis was performed as described in our previous work (*44*, *67*). Briefly, the average sarcomere length was defined as spacing between TnI striations from black and white renderings of ×60 magnification confocal graft images. Using ImageJ, fluorescence profiles along lines passing perpendicular through three different striated regions containing at least six consecutive sarcomere structures were measured and divided by the total number of sarcomeres. Z-line width was measured on TnI-stained graft images by measuring the width of striations from the same regions described above.

Cardiomyocyte alignment

hPSC-CMs were identified in vitro and in vivo via the presence of αSA or TnI, respectively. To quantify cardiomyocyte alignment, the 2D orientation order parameter (OOP) was determined as done by others (*71*, *72*), calculated via the equation below

$$\mathrm{OOP} = 2(\langle \cos^2(\theta - \mu_0) \rangle) - 1/2$$

where θ is the cardiomyocyte orientation angle and μ_0 is the mean orientation angle of the cardiomyocytes considered. In this system, OOP ranges from 0 to 1, indicating random orientation or perfect orientation, respectively. Cardiomyocyte orientation angles used in 2D OOP calculations were determined in ImageJ with standard plugins. The individual angle measurements corresponded to adjacent cardiomyocytes in 75 μm by 75 μm regions of in vitro cardiac organoids or in vivo engraftments of cardiac organoids.

Assessment of cardiac hypertrophy

Cardiomyocyte cross-sectional area was determined via staining of cell boundaries with Alexa Fluor 488–conjugated WGA (Invitrogen). Slides were incubated with WGA (10 μg/ml) for 20 min at room temperature and washed with PBS three times before coverslipping. To quantify the cell size, three independent samples per group with three different regions of interest from the border and remote zones in the left ventricle were captured at ×40 magnification with a TCS SP5 AOBS laser scanning confocal microscope (Leica Microsystems). Images were binarized in ImageJ and the Analyze Particles function was used to quantify individual cardiomyocyte area.

Statistical analysis

Statistical testing was performed using one- or two-tailed *t* tests where applicable, as stated in figure legends. Paired *t* tests were used when applicable for paired groups. Normal distribution of values was confirmed using the Shapiro-Wilk normality test where appropriate. The variance between samples was tested with an *F* test for equal variance. The Student's *t* test was used if the group variance was equal, and a Mann-Whitney nonparametric test was applied for groups with unequal variance. Bonferroni correction was used to adjust for multiple corrections. Statistical significance was determined by $P < 0.05$ unless otherwise stated.

Supplementary Materials

This PDF file includes:

Figs. S1 to S16
Tables S1 to S3

REFERENCES AND NOTES

1. E. J. Benjamin, P. Muntner, A. Alonso, M. S. Bittencourt, C. W. Callaway, A. P. Carson, A. M. Chamberlain, A. R. Chang, S. Cheng, S. R. Das, F. N. Delling, L. Djousse, M. S. V. Elkind, J. F. Ferguson, M. Fornage, L. C. Jordan, S. S. Khan, B. M. Kissela, K. L. Knutson, T. W. Kwan, D. T. Lackland, T. T. Lewis, J. H. Lichtman, C. T. Longenecker, M. S. Loop, P. L. Lutsey, S. S. Martin, K. Matsushita, A. E. Moran, M. E. Mussolino, M. O'Flaherty, A. Pandey, A. M. Perak, W. D. Rosamond, G. A. Roth, U. K. A. Sampson, G. M. Satou, E. B. Schroeder, S. H. Shah, N. L. Spartano, A. Stokes, D. L. Tirschwell, C. W. Tsao, M. P. Turakhia, L. B. Van Wagner, J. T. Wilkins, S. S. Wong, S. S. Virani; American Heart Association Council on Epidemiology and Prevention Statistics Committee and Stroke Statistics Subcommittee, Heart disease and stroke statistics-2019 update: A report from the American Heart Association. *Circulation* **139**, e56–e528 (2019).
2. O. Bergmann, S. Zdunek, A. Felker, M. Salehpour, K. Alkass, S. Bernard, S. L. Sjostrom, M. Szewczykowska, T. Jackowska, C. dos Remedios, T. Malm, M. Andrä, R. Jashari, J. R. Nyengaard, G. Possnert, S. Jovinge, H. Druid, J. Frisén, Dynamics of cell generation and turnover in the human heart. *Cell* **161**, 1566–1575 (2015).
3. C. E. Murry, H. Reinecke, L. M. Pabon, Regeneration gaps: Observations on stem cells and cardiac repair. *J. Am. Coll. Cardiol.* **47**, 1777–1785 (2006).
4. W.-Z. Zhu, K. D. Hauch, C. Xu, M. A. Laflamme, Human embryonic stem cells and cardiac repair. *Transplant. Rev.* **23**, 53–68 (2009).
5. P. Menasché, Stem cells for clinical use in cardiovascular medicine: Current limitations and future perspectives. *Thromb. Haemost.* **94**, 697–701 (2005).
6. M. N. Hirt, A. Hansen, T. Eschenhagen, Cardiac tissue engineering: State of the art. *Circ. Res.* **114**, 354–367 (2014).
7. G. Vunjak-Novakovic, N. Tandon, A. Godier, R. Maidhof, A. Marsano, T. P. Martens, M. Radisic, Challenges in cardiac tissue engineering. *Tissue Eng. Part B Rev.* **16**, 169–187 (2010).
8. X. Lian, C. Hsiao, G. Wilson, K. Zhu, L. B. Hazeltine, S. M. Azarin, K. K. Raval, J. Zhang, T. J. Kamp, S. P. Palecek, Robust cardiomyocyte differentiation from human pluripotent stem cells via temporal modulation of canonical Wnt signaling. *Proc. Natl. Acad. Sci. U.S.A.* **109**, E1848–E1857 (2012).
9. S. Funakoshi, K. Miki, T. Takaki, C. Okubo, T. Hatani, K. Chonabayashi, M. Nishikawa, I. Takei, A. Oishi, M. Narita, M. Hoshijima, T. Kimura, S. Yamanaka, Y. Yoshida, Enhanced engraftment, proliferation, and therapeutic potential in heart using optimized human iPSC-derived cardiomyocytes. *Sci. Rep.* **6**, 19111 (2016).
10. M. A. Laflamme, K. Y. Chen, A. V. Naumova, V. Muskheli, J. A. Fugate, S. K. Dupras, H. Reinecke, C. Xu, M. Hassanipour, S. Police, C. O'Sullivan, L. Collins, Y. Chen, E. Minami, E. A. Gill, S. Ueno, C. Yuan, J. Gold, C. E. Murry, Cardiomyocytes derived from human embryonic stem cells in pro-survival factors enhance function of infarcted rat hearts. *Nat. Biotechnol.* **25**, 1015–1024 (2007).
11. F. Weinberger, K. Breckwoldt, S. Pecha, A. Kelly, B. Geertz, J. Starbatty, T. Yorgan, K.-H. Cheng, K. Lessmann, T. Stolen, M. Scherrer-Crosbie, G. Smith, H. Reichenspurner, A. Hansen, T. Eschenhagen, Cardiac repair in Guinea pigs with human engineered heart tissue from induced pluripotent stem cells. *Sci. Transl. Med.* **8**, 363ra148 (2016).
12. Y. Shiba, S. Fernandes, W.-Z. Zhu, D. Filice, V. Muskheli, J. Kim, N. J. Palpant, J. Gantz, K. W. Moyes, H. Reinecke, B. van Biber, T. Dardas, J. L. Mignone, A. Izawa, R. Hanna, M. Viswanathan, J. D. Gold, M. I. Kotlikoff, N. Sarvazyan, M. W. Kay, C. E. Murry, M. A. Laflamme, Human ES-cell-derived cardiomyocytes electrically couple and suppress arrhythmias in injured hearts. *Nature* **489**, 322–325 (2012).

13. L. Ye, Y.-H. Chang, Q. Xiong, P. Zhang, L. Zhang, P. Somasundaram, M. Lepley, C. Swingen, L. Su, J. S. Wendel, J. Guo, A. Jang, D. Rosenbush, L. Greder, J. R. Dutton, J. Zhang, T. J. Kamp, D. S. Kaufman, Y. Ge, J. Zhang, Cardiac repair in a porcine model of acute myocardial infarction with human induced pluripotent stem cell-derived cardiovascular cells. *Cell Stem Cell* **15**, 750–761 (2014).
14. M. Ishida, S. Miyagawa, A. Saito, S. Fukushima, A. Harada, E. Ito, F. Ohashi, T. Watabe, J. Hatazawa, K. Matsuura, Y. Sawa, Transplantation of human-induced pluripotent stem cell-derived cardiomyocytes is superior to somatic stem cell therapy for restoring cardiac function and oxygen consumption in a porcine model of myocardial infarction. *Transplantation* **103**, 291–298 (2019).
15. Y. Shiba, T. Gomibuchi, T. Seto, Y. Wada, H. Ichimura, Y. Tanaka, T. Ogasawara, K. Okada, N. Shiba, K. Sakamoto, D. Ido, T. Shiina, M. Ohkura, J. Nakai, N. Uno, Y. Kazuki, M. Oshimura, I. Minami, U. Ikeda, Allogeneic transplantation of iPS cell-derived cardiomyocytes regenerates primate hearts. *Nature* **538**, 388–391 (2016).
16. Y.-W. Liu, B. Chen, X. Yang, J. A. Fugate, F. A. Kalucki, A. Futakuchi-Tsuchida, L. Couture, K. W. Vogel, C. A. Astley, A. Baldessari, J. Ogle, C. W. Don, Z. L. Steinberg, S. P. Seslar, S. A. Tuck, H. Tsuchida, A. V. Naumova, S. K. Dupras, M. S. Lyu, J. Lee, D. W. Hailey, H. Reinecke, L. Pabon, B. H. Fryer, W. R. MacLellan, R. S. Thies, C. E. Murry, Human embryonic stem cell-derived cardiomyocytes restore function in infarcted hearts of non-human primates. *Nat. Biotechnol.* **36**, 597–605 (2018).
17. J. J. H. Chong, X. Yang, C. W. Don, E. Minami, Y.-W. Liu, J. J. Weyers, W. M. Mahoney, B. Van Biber, S. M. Cook, N. J. Palpant, J. A. Gantz, J. A. Fugate, V. Muskheli, G. M. Gough, K. W. Vogel, C. A. Astley, C. E. Hotchkiss, A. Baldessari, L. Pabon, H. Reinecke, E. A. Gill, V. Nelson, H.-P. Kiem, M. A. Laflamme, C. E. Murry, Human embryonic-stem-cell-derived cardiomyocytes regenerate non-human primate hearts. *Nature* **510**, 273–277 (2014).
18. T. E. Robey, M. K. Saiget, H. Reinecke, C. E. Murry, Systems approaches to preventing transplanted cell death in cardiac repair. *J. Mol. Cell. Cardiol.* **45**, 567–581 (2008).
19. J. Zhang, W. Zhu, M. Radisic, G. Vunjak-Novakovic, Can we engineer a human cardiac patch for therapy? *Circ. Res.* **123**, 244–265 (2018).
20. R. Cruz-Acuña, M. Quirós, A. E. Farkas, P. H. Dedhia, S. Huang, D. Siuda, V. García-Hernández, A. J. Miller, J. R. Spence, A. Nusrat, A. J. García, Synthetic hydrogels for human intestinal organoid generation and colonic wound repair. *Nat. Cell Biol.* **19**, 1326–1335 (2017).
21. S. Yui, T. Nakamura, T. Sato, Y. Nemoto, T. Mizutani, X. Zheng, S. Ichinose, T. Nagaishi, R. Okamoto, K. Tsuchiya, H. Clevers, M. Watanabe, Functional engraftment of colon epithelium expanded in vitro from a single adult Lgr5+ stem cell. *Nat. Med.* **18**, 618–623 (2012).
22. C. L. Watson, M. M. Mahe, J. Múnera, J. C. Howell, N. Sundaram, H. M. Poling, J. I. Schweitzer, J. E. Vallance, C. N. Mayhew, Y. Sun, G. Grabowski, S. R. Finkbeiner, J. R. Spence, N. F. Shroyer, J. M. Wells, M. A. Helmrath, An in vivo model of human small intestine using pluripotent stem cells. *Nat. Med.* **20**, 1310–1314 (2014).
23. F. Lebreton, V. Lavallard, K. Bellofatto, R. Bonnet, C. H. Wassmer, L. Perez, V. Kalandadze, A. Follenzi, M. Boulvain, J. Kerr-Conte, D. J. Goodman, D. Bosco, T. Berney, E. Berishvili, Insulin-producing organoids engineered from islet and amniotic epithelial cells to treat diabetes. *Nat. Commun.* **10**, 4491 (2019).
24. Y.-Z. Nie, Y.-W. Zheng, M. Ogawa, E. Miyagi, H. Taniguchi, Human liver organoids generated with single donor-derived multiple cells rescue mice from acute liver failure. *Stem Cell Res. Ther.* **9**, 5 (2018).
25. B. T. McLelland, B. Lin, A. Mathur, R. B. Aramant, B. B. Thomas, G. Nistor, H. S. Keirstead, M. J. Seiler, Transplanted hESC-derived retina organoid sheets differentiate, integrate, and improve visual function in retinal degenerate rats. *Invest. Ophthalmol. Vis. Sci.* **59**, 2586–2603 (2018).
26. S.-N. Wang, Z. Wang, T.-Y. Xu, M.-H. Cheng, W.-L. Li, C.-Y. Miao, Cerebral organoids repair ischemic stroke brain injury. *Transl. Stroke Res.* **11**, 983–1000 (2020).
27. D. Jgamadze, J. T. Lim, Z. Zhang, P. M. Harary, J. Germi, K. Mensah-Brown, C. D. Adam, E. Mirzakhalili, S. Singh, J. B. Gu, R. Blue, M. Dedhia, M. Fu, F. Jacob, X. Qian, K. Gagnon, M. Sergison, O. Fruchet, I. Rahaman, H. Wang, F. Xu, R. Xiao, D. Contreras, J. A. Wolf, H. Song, G.-L. Ming, H.-C. I. Chen, Structural and functional integration of human forebrain organoids with the injured adult rat visual system. *Cell Stem Cell* **30**, 137–152.e7 (2023).
28. A. I. Weiner, S.R. Jackson, G. Zhao, K.K. Quansah, J.N. Farshchian, K.M. Neupauer, E.Q. Littauer, A.J. Paris, D.C. Liberti, G.S. Worthen, E.E. Morrisey, A.E. Vaughan, Mesenchyme-free expansion and transplantation of adult alveolar progenitor cells: Steps toward cell-based regenerative therapies. *NPJ Regen. Med.* **4**, 17 (2019).
29. D. J. Richards, Y. Li, C. M. Kerr, J. Yao, G. C. Beeson, R. C. Coyle, X. Chen, J. Jia, B. Damon, R. Wilson; E Starr Hazard, G. Hardiman, D. R. Menick, C. C. Beeson, H. Yao, T. Ye, Y. Mei, Human cardiac organoids for the modelling of myocardial infarction and drug cardiotoxicity. *Nat. Biomed. Eng.* **4**, 446–462 (2020).
30. L. Wang, Y. Liu, G. Ye, Y. He, B. Li, Y. Guan, B. Gong, K. Mequanint, M. M. Q. Xing, X. Qiu, Injectable and conductive cardiac patches repair infarcted myocardium in rats and minipigs. *Nat. Biomed. Eng.* **5**, 1157–1173 (2021).
31. F. Munarin, R. J. Kant, C. E. Rupert, A. Khoo, K. L. K. Coulombe, Engineered human myocardium with local release of angiogenic proteins improves vascularization and cardiac function in injured rat hearts. *Biomaterials* **251**, 120033 (2020).
32. A. Lesman, M. Habib, O. Caspi, A. Gepstein, G. Arbel, S. Levenberg, L. Gepstein, Transplantation of a tissue-engineered human vascularized cardiac muscle. *Tissue Eng. Part A* **16**, 115–125 (2010).
33. L. Gao, Z. R. Gregorich, W. Zhu, S. Mattapally, Y. Oduk, X. Lou, R. Kannappan, A. V. Borovjagin, G. P. Walcott, A. E. Pollard, V. G. Fast, X. Hu, S. G. Lloyd, Y. Ge, J. Zhang, Large cardiac muscle patches engineered from human induced-pluripotent stem cell-derived cardiac cells improve recovery from myocardial infarction in swine. *Circulation* **137**, 1712–1730 (2018).
34. S. Kawaguchi, Y. Soma, K. Nakajima, H. Kanazawa, S. Tohyama, R. Tabei, A. Hirano, N. Handa, Y. Yamada, S. Okuda, S. Hishikawa, T. Teratani, S. Kunita, Y. Kishino, M. Okada, S. Tanosaki, S. Someya, Y. Morita, H. Tani, Y. Kawai, M. Yamazaki, A. Ito, R. Shibata, T. Murohara, Y. Tabata, E. Kobayashi, H. Shimizu, K. Fukuda, J. Fujita, Intramyocardial transplantation of human iPS cell–derived cardiac spheroids improves cardiac function in heart failure animals. *JACC: Basic Transl. Sci.* **6**, 239–254 (2021).
35. J. Riegler, M. Tiburcy, A. Ebert, E. Tzatzalos, U. Raaz, O. J. Abilez, Q. Shen, N. G. Kooreman, E. Neofytou, V. C. Chen, M. Wang, T. Meyer, P. S. Tsao, A. J. Connolly, L. A. Couture, J. D. Gold, W. H. Zimmermann, J. C. Wu, Human engineered heart muscles engraft and survive long term in a rodent myocardial infarction model. *Circ. Res.* **117**, 720–730 (2015).
36. K. Yee, K. Malliaras, H. Kanazawa, E. Tseliou, K. Cheng, D. J. Luthringer, C.-S. Ho, K. Takayama, N. Minamino, J. F. Dawkins, S. Chowdhury, D. T. Duong, J. Seinfeld, R. C. Middleton, R. Dharmakumar, D. Li, L. Marbán, R. R. Makkar, E. Marbán, Allogeneic cardiospheres delivered via percutaneous transendocardial injection increase viable myocardium, decrease scar size, and attenuate cardiac dilatation in porcine ischemic cardiomyopathy. *PLOS ONE* **9**, –e113805 (2014).
37. M. Y. Emmert, P. Wolint, S. Winklhofer, P. Stolzmann, N. Cesarovic, T. Fleischmann, T. D. L. Nguyen, T. Frauenfelder, R. Böni, J. Scherman, D. Bettex, J. Grünenfelder, R. Schwartlander, V. Vogel, M. Gyöngyösi, H. Alkadhi, V. Falk, S. P. Hoerstrup, Transcatheter based electromechanical mapping guided intramyocardial transplantation and in vivo tracking of human stem cell based three dimensional microtissues in the porcine heart. *Biomaterials* **34**, 2428–2441 (2013).
38. D. J. Richards, R. C. Coyle, Y. Tan, J. Jia, K. Wong, K. Toomer, D. R. Menick, Y. Mei, Inspiration from heart development: Biomimetic development of functional human cardiac organoids. *Biomaterials* **142**, 112–123 (2017).
39. K. Ashtari, H. Nazari, H. Ko, P. Tebon, M. Akhshik, M. Akbari, S. N. Alhosseini, M. Mozafari, B. Mehravi, M. Soleimani, R. Ardehali, M. Ebrahimi Warkiani, S. Ahadian, A. Khademhosseini, Electrically conductive nanomaterials for cardiac tissue engineering. *Adv. Drug Deliv. Rev.* **144**, 162–179 (2019).
40. T. Dvir, B. P. Timko, M. D. Brigham, S. R. Naik, S. S. Karajanagi, O. Levy, H. Jin, K. K. Parker, R. Langer, D. S. Kohane, Nanowired three-dimensional cardiac patches. *Nat. Nanotechnol.* **6**, 720–725 (2011).
41. M. A. Tölli, M. P. A. Ferreira, S. M. Kinnunen, J. Rysä, E. M. Mäkilä, Z. Szabó, R. E. Serpi, P. J. Ohukainen, M. J. Välimäki, A. M. R. Correia, J. J. Salonen, J. T. Hirvonen, H. J. Ruskoaho, H. A. Santos, *In vivo* biocompatibility of porous silicon biomaterials for drug delivery to the heart. *Biomaterials* **35**, 8394–8405 (2014).
42. J. F. Zimmerman, R. Parameswaran, G. Murray, Y. Wang, M. Burke, B. Tian, Cellular uptake and dynamics of unlabeled freestanding silicon nanowires. *Sci. Adv.* **2**, e1601039 (2016).
43. V. Schmidt, J. V. Wittemann, U. Gösele, Growth, thermodynamics, and electrical properties of silicon nanowires. *Chem. Rev.* **110**, 361–388 (2010).
44. Y. Tan, D. Richards, R. Xu, S. Stewart-Clark, S. K. Mani, T. K. Borg, D. R. Menick, B. Tian, Y. Mei, Silicon nanowire-induced maturation of cardiomyocytes derived from human induced pluripotent stem cells. *Nano Lett.* **15**, 2765–2772 (2015).
45. Y. Tan, D. Richards, R. C. Coyle, J. Yao, R. Xu, W. Gou, H. Wang, D. R. Menick, B. Tian, Y. Mei, Cell number per spheroid and electrical conductivity of nanowires influence the function of silicon nanowired human cardiac spheroids. *Acta Biomater.* **51**, 495–504 (2017).
46. D. J. Richards, Y. Tan, R. Coyle, Y. Li, R. Xu, N. Yeung, A. Parker, D. R. Menick, B. Tian, Y. Mei, Nanowires and electrical stimulation synergistically improve functions of hiPSC cardiac spheroids. *Nano Lett.* **16**, 4670–4678 (2016).
47. K. A. Gerbin, X. Yang, C. E. Murry, K. L. Coulombe, Enhanced electrical integration of engineered human myocardium via intramyocardial versus epicardial delivery in infarcted rat hearts. *PLOS ONE* **10**, e0131446 (2015).
48. M. A. Laflamme, J. Gold, C. Xu, M. Hassanipour, E. Rosler, S. Police, V. Muskheli, C. E. Murry, Formation of human myocardium in the rat heart from human embryonic stem cells. *Am. J. Pathol.* **167**, 663–671 (2005).
49. A. von Gise, W. T. Pu, Endocardial and epicardial epithelial to mesenchymal transitions in heart development and disease. *Circ. Res.* **110**, 1628–1645 (2012).
50. E. Giacomelli, V. Meraviglia, G. Campostrini, A. Cochrane, X. Cao, R. W. J. van Helden, A. Krotenberg Garcia, M. Mircea, S. Kostidis, R. P. Davis, B. J. van Meer, C. R. Jost, A. J. Koster,

H. Mei, D. G. Míguez, A. A. Mulder, M. Ledesma-Terrón, G. Pompilio, L. Sala, D. C. F. Salvatori, R. C. Slieker, E. Sommariva, A. A. F. de Vries, M. Giera, S. Semrau, L. G. J. Tertoolen, V. V. Orlova, M. Bellin, C. L. Mummery, Human-iPSC-derived cardiac stromal cells enhance maturation in 3d cardiac microtissues and reveal non-cardiomyocyte contributions to heart disease. *Cell Stem Cell* **26**, 862–879.e11 (2020).

51. S. Fernandes, J. J. H. Chong, S. L. Paige, M. Iwata, B. Torok-Storb, G. Keller, H. Reinecke, C. E. Murry, Comparison of human embryonic stem cell-derived cardiomyocytes, cardiovascular progenitors, and bone marrow mononuclear cells for cardiac repair. *Stem Cell Reports* **5**, 753–762 (2015).
52. M. Zhang, D. Methot, V. Poppa, Y. Fujio, K. Walsh, C. E. Murry, Cardiomyocyte grafting for cardiac repair: Graft cell death and anti-death strategies. *J. Mol. Cell. Cardiol.* **33**, 907–921 (2001).
53. R. Romagnuolo, H. Masoudpour, A. Porta-Sánchez, B. Qiang, J. Barry, A. Laskary, X. Qi, S. Massé, K. Magtibay, H. Kawajiri, J. Wu, T. V. Sadikov, J. Rothberg, K. M. Panchalingam, E. Titus, R.-K. Li, P. W. Zandstra, G. A. Wright, K. Nanthakumar, N. R. Ghugre, G. Keller, M. A. Laflamme, Human embryonic stem cell-derived cardiomyocytes regenerate the infarcted pig heart but induce ventricular tachyarrhythmias. *Stem Cell Reports* **12**, 967–981 (2019).
54. J. S. Burchfield, M. Xie, J. A. Hill, Pathological ventricular remodeling. *Circulation* **128**, 388–400 (2013).
55. C. Peet, A. Ivetic, D. I. Bromage, A. M. Shah, Cardiac monocytes and macrophages after myocardial infarction. *Cardiovasc. Res.* **116**, 1101–1112 (2020).
56. T. Ogasawara, S. Okano, H. Ichimura, S. Kadota, Y. Tanaka, I. Minami, M. Uesugi, Y. Wada, N. Saito, K. Okada, K. Kuwahara, Y. Shiba, Impact of extracellular matrix on engraftment and maturation of pluripotent stem cell-derived cardiomyocytes in a rat myocardial infarct model. *Sci. Rep.* **7**, 8630 (2017).
57. J. Bargehr, L. P. Ong, M. Colzani, H. Davaapil, P. Hofsteen, S. Bhandari, L. Gambardella, N. le Novère, D. Iyer, F. Sampaziotis, F. Weinberger, A. Bertero, A. Leonard, W. G. Bernard, A. Martinson, N. Figg, M. Regnier, M. R. Bennett, C. E. Murry, S. Sinha, Epicardial cells derived from human embryonic stem cells augment cardiomyocyte-driven heart regeneration. *Nat. Biotechnol.* **37**, 895–906 (2019).
58. C. E. Murry, W. R. MacLellan, Stem cells and the heart—The road ahead. *Science* **367**, 854–855 (2020).
59. R. Parameswaran, K. Koehler, M. Y. Rotenberg, M. J. Burke, J. Kim, K.-Y. Jeong, B. Hissa, M. D. Paul, K. Moreno, N. Sarma, T. Hayes, E. Sudzilovsky, H.-G. Park, B. Tian, Optical stimulation of cardiac cells with a polymer-supported silicon nanowire matrix. *Proc. Natl. Acad. Sci.* **116**, 413–421 (2019).
60. X. Zhao, H. Chen, D. Xiao, H. Yang, I. Itzhaki, X. Qin, T. Chour, A. Aguirre, K. Lehmann, Y. Kim, P. Shukla, A. Holmström, J. Z. Zhang, Y. Zhuge, B. C. Ndoye, M. Zhao, E. Neofytou, W.-H. Zimmermann, M. Jain, J. C. Wu, Comparison of non-human primate versus human induced pluripotent stem cell-derived cardiomyocytes for treatment of myocardial infarction. *Stem Cell Report* **10**, 422–435 (2018).
61. D. Schüttler, A. Bapat, S. Kääb, K. Lee, P. Tomsits, S. Clauss, W. J. Hucker, Animal models of atrial fibrillation. *Circ. Res.* **127**, 91–110 (2020).
62. S. Kaese, S. Verheule, Cardiac electrophysiology in mice: A matter of size. *Front. Physiol.* **3**, 345 (2012).
63. J. K. Yu, W. Franceschi, Q. Huang, F. Pashakhanloo, P. M. Boyle, N. A. Trayanova, A comprehensive, multiscale framework for evaluation of arrhythmias arising from cell therapy in the whole post-myocardial infarcted heart. *Sci. Rep.* **9**, 9238 (2019).
64. Y. Xie, D. Sato, A. Garfinkel, Z. Qu, J. N. Weiss, So little source, so much sink: Requirements for afterdepolarizations to propagate in tissue. *Biophys. J.* **99**, 1408–1415 (2010).
65. A. N. Plotnikov, I. Shlapakova, M. J. Szabolcs, P. Danilo Jr., B. H. Lorell, I. A. Potapova, Z. Lu, A. B. Rosen, R. T. Mathias, P. R. Brink, R. B. Robinson, I. S. Cohen, M. R. Rosen, Xenografted adult human mesenchymal stem cells provide a platform for sustained biological pacemaker function in canine heart. *Circulation* **116**, 706–713 (2007).
66. Z. Wu, H. Zhuang, B. Ma, Y. Xiao, B. Koc, Y. Zhu, C. Wu, Manganese-doped calcium silicate nanowire composite hydrogels for melanoma treatment and wound healing. *Research (Washington, D.C.)* **2021**, 9780943 (2021).
67. Y. Tan, all dissertations, Clemson University (2017).
68. D. J. Richards, all dissertations, Clemson University (2018).
69. R. C. Coyle, R. W. Barrs, D. J. Richards, E. P. Ladd, D. R. Menick, Y. Mei, Targeting HIF-α for robust prevascularization of human cardiac organoids. *J. Tissue Eng. Regen. Med.* **15**, 189–202 (2021).
70. C. A. Schneider, W. S. Rasband, K. W. Eliceiri, NIH image to ImageJ: 25 years of image analysis. *Nat. Methods* **9**, 671–675 (2012).
71. A. Umeno, S. Ueno, Quantitative analysis of adherent cell orientation influenced by strong magnetic fields. *IEEE Trans. Nanobioscience* **2**, 26–28 (2003).
72. A. W. Feinberg, P. W. Alford, H. Jin, C. M. Ripplinger, A. A. Werdich, S. P. Sheehy, A. Grosberg, K. K. Parker, Controlling the contractile strength of engineered cardiac muscle by hierarchal tissue architecture. *Biomaterials* **33**, 5732–5741 (2012).

Acknowledgments

Funding: This work was supported by NIH grant 8P20 GM103444 (to Y.M.), NIH grant U54 GM104941 (to Y.M.), NIH grant R01HL133308 (to Y.M.), NIH grant F31 HL145979 (to R.C.C.), NIH grant F31 HL156541 (to R.W.B.), Startup funds from Clemson University (to Y.M.), National Science Foundation grant EPS-0903795 (to Y.M.), National Science Foundation grant DMR-2105321 (to B.T.), NIH Cardiovascular Training Grant T32 HL007260 (to D.R.M.), and U.S. Department of Veterans Affairs Merit Review grant I01 BX002327 (to D.R.M.), This study used the services of the Morphology, Imaging, and Instrumentation Core, which is supported by NIH-NIGMS grant P30 GM103342 to the South Carolina COBRE for Developmentally Based Cardiovascular Diseases. **Author contributions:** Conceptualization: All authors. Methodology: All authors. Investigation: Y.T., R.C.C., R.W.B., S.E.S., and M.L. Visualization: Y.T., R.C.C., R.W.B., S.E.S., M.L., D.J.R., and Y.M. Supervision: Y.M. Writing—original draft: Y.T., R.C.C., R.W.B., and Y.M. Writing—review and editing: Y.T., R.C.C., R.W.B., S.E.S., M.L., D.R.M., B.T., and Y.M. **Competing interests:** Y.M., Y.T., D.J.R., D.R.M., and B.T. are inventors on a patent related to this work filed by University of Chicago, MUSC Foundation for Research Development, Clemson University Research Foundation (CURF) (no. US10988735B2, filed 15 January 2016, published 27 April 2021). Y.M. and D.J.R. are inventors on a pending patent related to this work filed by Clemson University Research Foundation (CURF) (no. US20220162559A1, filed 9 July 2019, published 26 May 2022). The authors declare that they have no other competing interests. **Data and materials availability:** Materials used in this research can be provided by Y.M. pending scientific review and a completed material transfer agreement. Requests for materials should be submitted to Y.M. All data needed to evaluate the conclusions in the paper are present in the paper and/or the Supplementary Materials.

Submitted 15 December 2022
Accepted 6 July 2023
Published 4 August 2023
10.1126/sciadv.adf2898

ScienceAdvances

Nanowired human cardiac organoid transplantation enables highly efficient and effective recovery of infarcted hearts

Yu Tan, Robert C. Coyle, Ryan W. Barrs, Sophia E. Silver, Mei Li, Dylan J. Richards, Yiliang Lin, Yuanwen Jiang, Hongjun Wang, Donald R. Menick, Kristine Deleon-Pennell, Bozhi Tian, and Ying Mei

Sci. Adv., **9** (31), eadf2898.
DOI: 10.1126/sciadv.adf2898